ECS Journal of Solid State
Science and Technology

Recent Advances and Challenges in Obtaining Stable $CsPbX_3$ (X = Cl, Br, and I) Nanocrystals Toward White Light-Emitting Applications

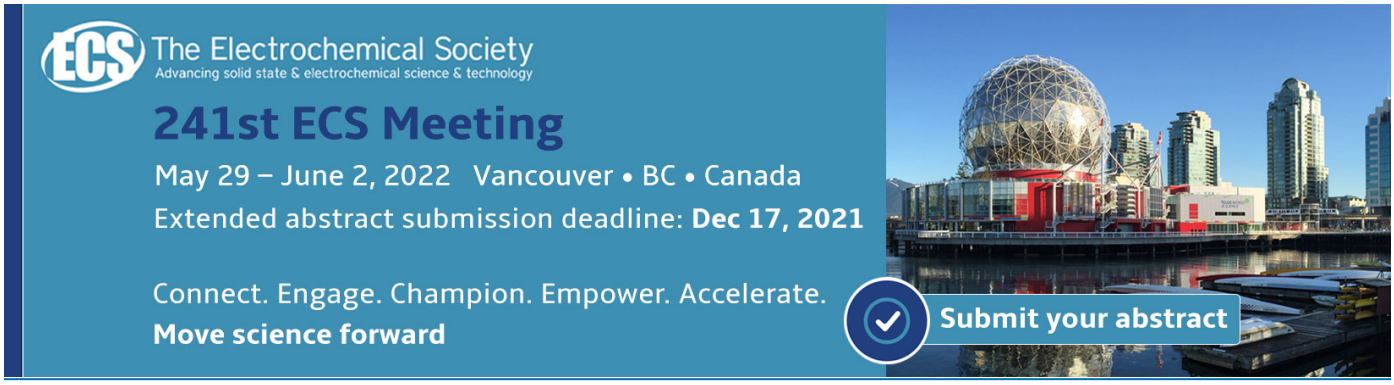

ECS Journal of Solid State Science and Technology, 2021 **10** 106001
2162-8777/2021/10(10)/106001/22/$40.00 © 2021 The Electrochemical Society ("ECS"). Published on behalf of ECS by IOP Publishing Limited

Recent Advances and Challenges in Obtaining Stable $CsPbX_3$ (X = Cl, Br, and I) Nanocrystals Toward White Light-Emitting Applications

G. Krishnamurthy Grandhi,[1,3] Krishnaiah Mokurala,[2,3] Joo Hyeong Han,[1] Han Bin Cho,[1] Ju Yeon Han,[1] and Won Bin Im[1,z]

[1]*Division of Materials Science and Engineering, Hanyang University, Seongdong-gu, Seoul 04763, Republic of Korea*
[2]*Department of Electronics Engineering, Incheon National University, Incheon 406-772, Republic of Korea*

Inorganic halide perovskite ($CsPbX_3$, X = Cl, Br, and I) nanocrystals (PNCs) have been highly sought-after materials in recent years owing to their numerous applications in optoelectronic devices. One such application is white light generation for displays and low-cost light sources. Nevertheless, the poor structural and chemical stabilities of these NCs under environmental factors, such as moisture and oxygen, hinder the fabrication of white light-emitting devices. The improved stability of halide PNCs has been mainly achieved by encapsulating them in robust matrices such as oxide materials, inorganic glass, and metal–organic frameworks. This review summarizes how various encapsulating strategies improve the structural stability of halide PNCs and preserve their bright luminescence characteristics, which aids in the fabrication of high-power white light-emitting diodes. Considering that the NCs are characterized by an inorganic perovskite core and an organic surface layer, we discuss their various structural and surface aspects in this review.
 [DOI: 10.1149/2162-8777/ac28e4]

Manuscript submitted July 28, 2021; revised manuscript received September 14, 2021. Published October 1, 2021. *This paper is part of the JSS Focus Issue on Focus Issue Dedicated to the Memory of George Blasse: Recent Developments in Theory, Materials, and Applications of Luminescence.*

Lead halide perovskite nanocrystals (PNCs) are a fascinating class of semiconducting NCs owing to their low-cost preparation using various strategies,[1] highly tunable optoelectronic properties, and easy processability, thus making them desirable candidates for a wide variety of applications, such as photovoltaics, light-emitting diodes (LEDs), lasing, and photodetectors.[2–5] In addition to these applications, PNCs have been implemented in other exciting applications such as X-ray detectors, field-effect transistors, photocatalysis, and nonlinear optics.[6] The absorption and photoluminescence (PL) energies of PNCs can be tuned within the UV-NIR regime by simply tuning their chemical composition or their size and shape.[1,2] Moreover, the absence of mid-gap trap states (i.e., defect tolerance) in the band gap regime also helps NCs achieve very bright emission.[7] The near-unity emission of PNCs has been ascribed to bright triple excitons, which are uncommon in conventional semiconductor NCs.[8] Overall, lead halide PNCs exhibit near-unity PL quantum yield (PL QY) and hence nearly single exponential PL decay behavior, in contrast to the comparatively negligible PL QY (<0.1%) observed in their bulk counterparts.[9,10] Owing to the highly efficient light-emitting nature of these NCs, LEDs with external quantum efficiencies as high as 20% have been achieved.[11] Therefore, PNCs are highly sought-after materials for light-emitting applications. Nevertheless, PNCs experience structural degradation under various environmental conditions, such as moisture, oxygen, light, and heat, which greatly hinders their development toward practical applications.[12] Passivation layers are essential for encapsulating perovskite PNCs to improve stability and preserve their excellent optical properties, promoting stability in light display devices, and enhancing their performance.[13–15] Suitable moisture-impermeable rigid materials are required for effective passivation.[14,15] These materials should possess mechanically robust lattices, low diffusion rates, or airtight characteristics to prevent the degradation of luminescence properties by the vibration of the crystal lattice and external environmental conditions.[14] Typically, passivated PNCs can be anticipated to exhibit a synergistic result, preserving the characteristics of protective materials as well as the outstanding luminescence properties.[16] The robust luminescence properties of perovskite hybrids, ensured by robust and inert protective layers, promote their utility in solid-state and highly power-efficient white LEDs (WLEDs) (Scheme 1).[16]

This review summarizes the stabilization strategies of using various passivating matrices such as inorganic materials, inorganic glass frames, metal–organic frameworks (MOFs), and polymers that have been used to encapsulate PNCs for improving structural as well as luminescence stabilities. We also summarize how the stable emission properties obtained for PNC-hybrids enable WLED applications. Before discussing the encapsulation matrices that stabilize the NCs and their emission characteristics against the extrinsic degradation factors, we discuss the structural (intrinsic) aspects such as phase transitions in $CsPbX_3$ NCs and their surface-ligand chemistry, as the understanding of these features is crucial for developing NCs for any application.

Crystal Structure and Phase Transitions

The 3D crystal structures of 3D lead halide perovskites resemble that of an oxide-based perovskite ($CaTiO_3$), as shown in Fig. 1a. An infinitely extended 3D framework comprising corner-sharing MX_6 octahedra forms a halide perovskite structure. They can be expressed in general as AMX_3, where X is a halogen atom and M = Pb^{2+}. The cuboctahedra, 12-fold voids formed by the metal halide framework, are filled with cations (A-site) such as Cs^+, MA^+, and FA^+. The electrostatic interaction between the A-site cations and the metal halide (M-X) framework tightens and stabilizes the structure. A simple formula to determine whether a given halide composition forms a stable perovskite structure based on the radii of cations and anions is known as the Goldschmidt tolerance factor (t) (introduced by Goldschmidt in 1962).[18] The tolerance factor can be expressed as

$$t = \frac{r_A + r_X}{\sqrt{2}\,(r_M + r_X)}$$

where r_A, r_M, and r_X represent the ionic radii of the A-and M-site cations and the halide ion (X), respectively. Stable cubic perovskite structures have t values ranging from 0.9 to 1.0. For example, $MAPbI_3$ with $t = 0.95$ crystallizes in a cubic perovskite structure. The relatively lower values of t = 0.8–0.89 promote metal halide rotation (tilting), thereby producing lower-symmetry phases, such as tetragonal, orthorhombic, monoclinic, and rhombohedral structures. The extent of octahedral rotation depends on the material

[3]These authors contributed equally to this work.
[z]E-mail: imwonbin@hanyang.ac.kr

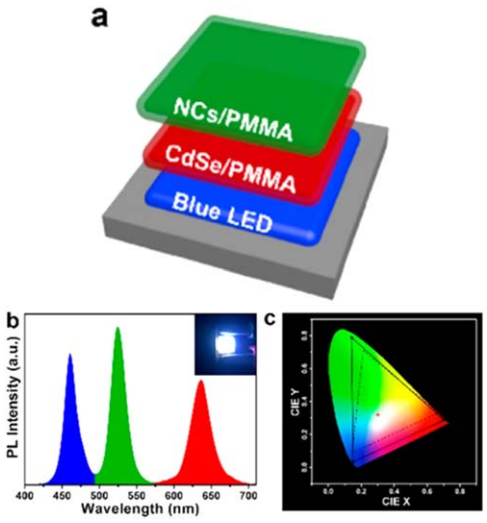

Scheme 1. (a) Schematic illustration of the configuration of the WLED device based on $CsPbBr_3/SiO_2$ NCs. (b) PL spectra of the WLED device (operating current level = 5 mA) and the inset shows a photograph of the WLED. (c) CIE color diagram of the WLED device.[17]

and Rb^+ are too small to form stable perovskite structures.[20] In addition, the octahedral factor (μ) determines the feasibility of a given M-site cation forming octahedra with a halide ion (X); the desirable range of μ is 0.4–0.9. A combination of μ and t, the parameter $(\mu + t)^{\eta}$, where η is the atomic packing fraction, is a better stability predictor, as it can predict the relative thermodynamic stability among any two perovskite structures with high accuracy.[21] For instance, $CsSnX_3$ NCs adopt a cubic perovskite structure in accordance with their tolerance factor of approximately 0.9. Nevertheless, they are unstable in air owing to the oxidation of Sn^{2+} to Sn^{4+}.[22]

Metal halides possess flexible and ionic crystal structures, which allow them to transform into various structural phases or different compositions. Biswas et al. demonstrated that cesium lead halides undergo postsynthetic structural (dimensional) transformations from 3D to 2D or 0D by a simple mechanochemical grinding approach under ambient conditions.[28] It should be noted that this flexible crystal structure can be found in lead-free metal halides, and a reversible postsynthetic transformation between 0D and 1D cesium copper iodides has been achieved by hand-grinding in the presence of excess CuI or CsI.[29] In contrast, cesium lead halides undergo various structural distortions owing to intrinsic or extrinsic factors. It is important to note that crystal (structural) defects and the size of halide PNCs are two important parameters that affect their structure.

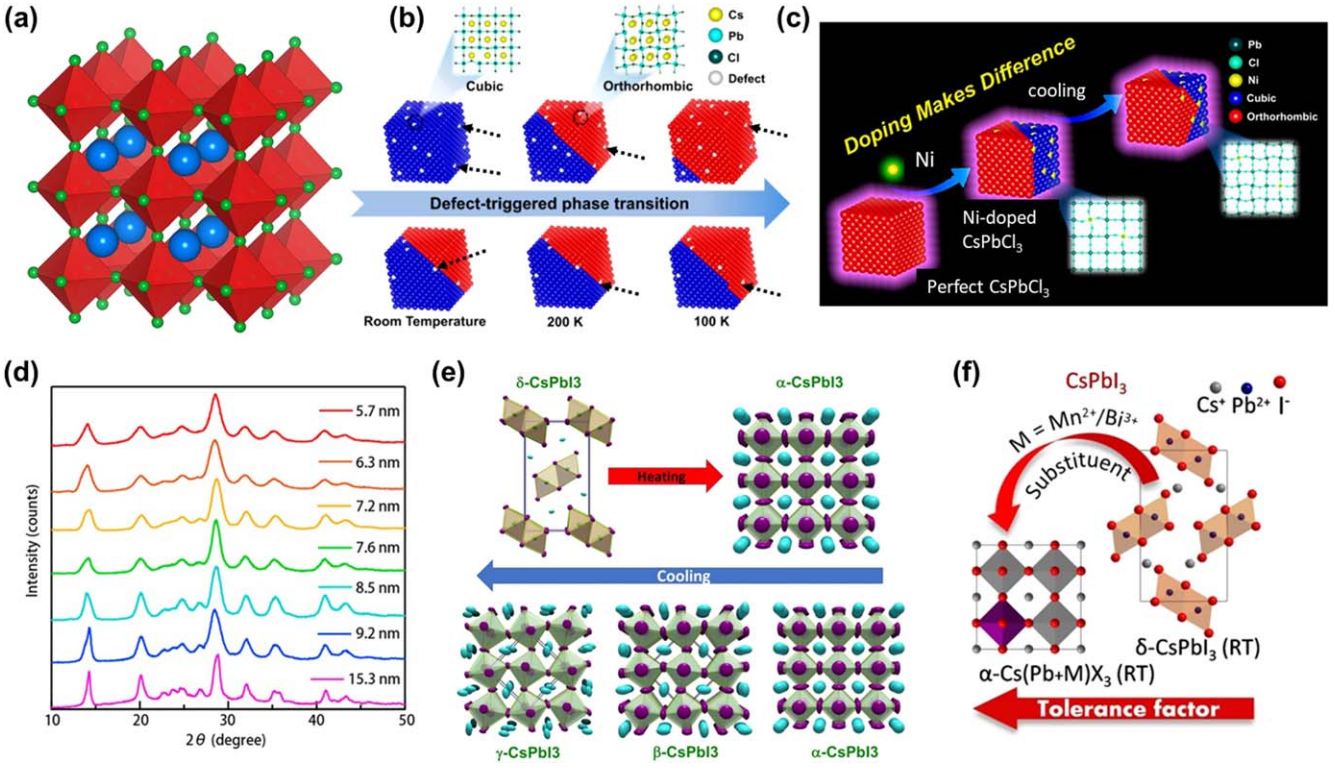

Figure 1. (a) 3D crystal structure of a typical lead halide perovskite of ABX_3 composition; the voids created by PbX_6^{4-} octahedra are occupied by Cs^+ ions. (b) In highly defective $CsPbCl_3$ NCs, the cubic subdomains gradually convert to orthorhombic upon cooling from room temperature, whereas defect-free NCs with mixed cubic and orthorhombic subdomains at room temperature display a significant resistance to the phase transition.[23] The dotted arrows indicate the defect sites on the NCs. (c) Ni^{2+} doping-induced hindered phase transition in $CsPbCl_3$ NCs.[24] (d) XRD patterns of $CsPbI_3$ NCs with increasing particle size (5.7–15.3 nm).[25] (e) Phase transitions in $CsPbI_3$: yellow δ-phase converts into black α-phase upon heating it beyond the transition temperature, and cooling reverts it to the yellow phase with three intermediate black phases.[26] (f) Partial substitution (doping or alloying) of the host Pb^{2+} by various metal ions can lead to stabilization of black phase $CsPbI_3$ NCs at room temperature by increasing its tolerance factor.[27]

composition. For example, octahedral tilting is lower in orthorhombic $CsPbBr_3$ ($t = 0.92$) than in orthorhombic $CsPbI_3$ ($t = 0.893$). If Cs^+ is replaced by much larger cations such as imidazolium, ethylamine, and guanidinium (GUA), they generate layered halide perovskites such as 2D $GUAPbI_4$[19]; here, $t = 1.039$ (>1) results in a layered structure formation. Monovalent cations such as Na^+, K^+,

Initially, halide PNCs exhibited certain structural discrepancies, as the same composition at room temperature was realized to crystallize in cubic, orthorhombic, and tetragonal phases based on simple X-ray diffraction (XRD) measurements. For instance, the high-intensity peaks in the XRD patterns of cubic and orthorhombic phases of $CsPbBr_3$ occur at the same Bragg angles, and the only

difference is the presence of a few additional low-intensity peaks between 20° and 30° in the case of orthorhombic $CsPbBr_3$. Therefore, it is difficult to assign the phase for nanosized $CsPbBr_3$ particles with a heavily broadened XRD pattern. In the initial literature reports, $CsPbBr_3$ NCs were thought to adopt a cubic phase based on the absence of low-intensity peaks (related to the orthorhombic phase) in the NC XRD pattern.[2] Differential scanning calorimetry (DSC) data of $CsPbBr_3$ NCs suggest an orthorhombic to tetragonal transition at approximately 91 °C and a tetragonal to cubic transition at approximately 132 °C.[30] This study proposed the appearance of $CsPbBr_3$ NCs in an orthorhombic polymorph at room temperature. Similarly, $CsPbI_3$ can exist in four different polymorphs, namely α-,β-,γ-, and δ-orthorhombic.[26] The first three phases are photoactive black phases, whereas the last phase is the nonperovskite (yellow) phase. The yellow phase is the most stable phase at room temperature; however, $CsPbI_3$ crystallizes in a metastable black phase. Black phase $CsPbI_3$ is widely believed to be trapped in an α-cubic perovskite polymorph. Rietveld refinement of the experimental XRD patterns of $CsPbI_3$ films and NCs verified that the material is trapped in the metastable γ-orthorhombic phase rather than the α-cubic phase.[25,31,32]

Owing to the relatively higher tolerance factor of $CsPbCl_3$, it is expected to form a cubic structure unlike $CsPbBr_3$ and $CsPbI_3$, which adopt an orthorhombic crystal structure at room temperature. X-ray total scattering data and modeling based on the Debye scattering equation prove that $CsPbCl_3$ NCs exist in the cubic phase.[33] Local crystal structure calculations show that $CsPbCl_3$ NCs contain a few subdomains with distorted lead chloride octahedra, suggesting that the NCs contain multiple orthorhombic nanodomains rather than existing solely in the cubic phase. Ma et al. presented an in-depth understanding of the phase transition in $CsPbCl_3$ NCs over a wide temperature range using Rietveld refinement of high-resolution synchrotron XRD patterns (collected at various temperatures) and molecular dynamic simulations.[23] The synchrotron XRD data revealed that the anion (chloride) vacancies (defects) not only determine the room temperature structure of the NCs, but also greatly affect their phase-transition behavior between cubic and orthorhombic forms. In this study, two types of NCs were chosen: defective $CsPbCl_3$ and high-quality $CsPbCl_3$ NCs (Fig. 1b). Defect less NCs show a higher fraction of orthorhombic polymorph, 48.4%, at room temperature, and the percentage increases to 75.3% upon cooling to 100 K. In contrast, the phase fraction of the orthorhombic polymorph in the defective NCs increases from 7.7% to 96.2% upon cooling it to 100 K, showing a nearly complete phase transition from the cubic to the orthorhombic polymorph. This defect-triggered phase transition in $CsPbCl_3$ NCs was verified by molecular dynamics calculations. In the case of crystals with defects, the Pb–Cl–Pb bonds undergo a strong fluctuation at 290 °C because the Cl vacancy leads to a strong lattice distortion in the surroundings. This local structural deformation releases the lattice strain and inhibits the lead chloride octahedral tilting, which in turn promotes the high-symmetry (cubic) crystal structure. The same study revealed that such defect-triggered phase transitions are possible with $CsPbBr_3$ NCs.[23]

Doping $CsPbCl_3$ NCs also strongly influences their phase-transition behavior. Ma et al. studied the effect of Ni^{2+} doping by synthesizing lightly (CPC-0.5Ni) and heavily doped (CPC-2Ni)-doped $CsPbCl_3$ NCs.[24] Ni^{2+} doping removes Cl vacancies by increasing their formation energy, resulting in a near-unity PL QY for CPC-2Ni. This suggests an almost defect-free CPC-2Ni lattice. In contrast, CPC-0.5Ni displayed a much lower PL QY (~4.2%), which is comparable to that of undoped $CsPbCl_3$ NCs (PL QY = ~1.2%), suggesting a higher concentration of chloride defects in the case of CPC-0.5Ni. CPC-0.5Ni is predominantly cubic at room temperature, and most of it transforms to an orthorhombic polymorph upon cooling. Nearly 89% of CPC-0.5Ni is orthorhombic at 100 K. In contrast, nearly defect-free CPC-2Ni enables the coexistence of both cubic and orthorhombic phases in equal proportions at room temperature. Molecular dynamics simulations revealed that the doping-triggered phase transition occurred because of the release of lattice strain upon Ni^{2+} doping (Fig. 1c).[24] Upon cooling, the orthorhombic polymorph percentage in CPC-2Ni increases only up to 77.3%, which is lower than that in the case of lightly doped NCs (CPC-0.5Ni), suggesting a hindered phase transition from the cubic to orthorhombic phase with a sufficient amount of doping (Fig. 1c). The constant tilting of the lead chloride octahedra with decreasing temperature is the cause of the temperature-insensitive phase transition in $CsPbCl_3$ NCs upon doping.

The particle size considerably influences the crystal structure and phase transition of $CsPbI_3$ NCs. Zhao et al. demonstrated the size-dependent crystal structure and the influence of surface energy on the stabilization of the structure of $CsPbI_3$ NCs by performing Rietveld refinement on experimentally obtained XRD patterns (Fig. 1d).[25] The XRD pattern of 5.3 nm $CsPbI_3$ NCs matched the α-cubic phase; however, a closer inspection revealed the presence of a broad peak at 23° (diffraction angle), which better describes the NCs in either the β-tetragonal or γ-orthorhombic phase. Therefore, owing to the broad XRD pattern, it became difficult to precisely assign the phase (between β-tetragonal or γ-orthorhombic or a mixture of α-, β-, and γ-phases) for smaller $CsPbI_3$ NCs. In contrast, the crystal phase of the larger particles matches well with the γ-orthorhombic phase, as evident from the XRD pattern. A relatively higher crystal symmetry (possibly a mixture of α-, β-, and γ-phases) of the smaller $CsPbI_3$ NCs indicates a lower lead iodide octahedral tilting on their surface, resulting from a lower lattice strain, arising from a higher surface energy of the smaller particles (−5.1 eV for 5.2 nm particles compared to −3.0 eV for 15.3 nm particles).[25] High-resolution TEM imaging revealed the size-dependent crystal structure of the $CsPbBr_3$ NCs.[34] While larger $CsPbBr_3$ particles coexist in both cubic and orthorhombic phases, cubic is the dominant phase for smaller $CsPbBr_3$ NCs.

The tolerance factor value of black phase $CsPbI_3$ is 0.893, because of which, the black phase is a metastable phase at room temperature (for comparison, room temperature-stable black phase $CsPbBr_3$ has a higher tolerance factor of 0.92). Therefore, the kinetically trapped black phase (α-, β-, or γ-phases) of $CsPbI_3$ NCs spontaneously (even in an inert atmosphere) converted into the yellow phase (δ-orthorhombic), which is the most stable phase at room temperature (Fig. 1e).[26,31] External factors such as light illumination, polar solvent treatment, and moisture exposure can promote the phase transition to δ-orthorhombic. Straus et al. demonstrated that γ-$CsPbI_3$ is stable under oxygen but rapidly transforms into δ-$CsPbI_3$ in the presence of moisture.[35] Another study showed that exposure to moisture led to their adsorption onto the $CsPbI_3$ surface and partially removed (dissolved) iodide anions. The higher concentration of halide vacancies lowers (catalyzes) the kinetic barrier between the black and yellow phases of $CsPbI_3$, resulting in a rapid transformation into the yellow phase.[36] Pressure applications also accelerate the phase transition in halide PNCs. Cao et al. found that the Pb–I–Pb bond angle is nearly 180° in $CsPbI_3$ NCs, but the Pb–I bond length decreases when applying pressure in the range 0–0.38 GPa.[37] As a result, the Pb-6s and I-5p orbitals become spatially closer and their interaction becomes stronger, resulting in a lower band gap of NCs (from 1.73 to 1.69 eV). However, applying a pressure >0.38 GPa results in a Pb–I–Pb bond angle of <180° and transforms the NCs from cubic to the orthorhombic phase (band gap increases to 1.79 eV). Similar pressure-triggered structural distortions were also observed in $CsPbBr_3$ NCs.[38] The highly polar solvents employed in the purification of halide PNCs also cause structural alterations. Sun et al. used a high-resolution STEM technique to study the effect of ethanol on the $CsPbI_3$ NC crystal structure.[39] Upon exposure to ethanol molecules, the lattice structure of the nanocubes undergoes distortion due to the migration of Cs^+ ions. Such lattice distortion induces dipole moments on the distorted nanocubes, which attract each other and self-assemble into single-crystalline $CsPbI_3$ nanowires. Consequently, a black to yellow phase transition occurs.[39]

Although approaches such as ligand engineering,[40] A-site doping,[41] and encapsulation with a high band gap matrix exist,[32] B-site doping with smaller cations (Cd^{2+}, Zn^{2+}, Mn^{2+}, Sr^{2+}, …) have been the most frequently applied strategies to stabilize $CsPbI_3$ NCs in the black phase. Manna et al. found that the incorporation of Mn^{2+} ions into the lattice of black phase $CsPbI_3$ NCs stabilized their crystal structure and prevented the phase transition into the yellow phase for more than a month.[42] The decelerated phase transition was attributed to a small decrease in the lattice volume upon Mn^{2+} doping, which slightly increased the Goldsmith tolerance factor, in addition to an increase in the cohesive energy. B-site doping (partially exchanging a few Pb^{2+} ions from the lattice of $CsPbI_3$ with relatively smaller cations) has typically been employed with the intention of reducing the average unit cell volume, which slightly increases the Goldsmith tolerance factor for improving the black phase stability (Fig. 1f).[27] Recently, Steele et al. demonstrated that deducing stability from reduction in unit cell volume alone is a deprived predictor of black phase stability.[43] For instance, because the ionic radius of the Ba^{2+} ion (1.35 Å) is larger than that of the host Pb^{2+} ion (1.19 Å), no improved phase stability can be anticipated when it is doped into the $CsPbI_3$ lattice. In contrast, Ba^{2+} doping has been shown to preserve the perovskite structure of $CsPbI_3$.[44] Moreover, some smaller dopants expand the unit cell volume instead of contracting it, and most B-site doped $CsPbI_3$ compositions were found to display nonlinear changes in volume, and hence, did not adhere to Vegard's law. In addition, external factors such as cooling rates, crystal size, NC surface chemistry, and other dynamic interactions must be considered to understand the phase-transition behavior. Steele et al., using Bi^{3+} doping as an example, demonstrated that the impurity-driven enhanced phase stability can be attributed to the suppression of spontaneous strain formation (explained in *the spontaneous strain model*) and increased crystal symmetry in the ambient environment.[43] This spontaneous strain model may experience divergence when dealing with $CsPbI_3$ particles <10 nm, owing the size-dependent changes in the crystal properties (lattice constants) of $CsPbI_3$ NCs.[25] In the case of encapsulation within high band gap matrix (i.e., Cs_4PbI_6), the improved phase stability of red-emitting γ-$CsPbI_3$ NCs has been attributed to the lowering of the Gibbs free energy of their transition to the δ-$CsPbI_3$ phase.[32] Currently, the $CsPbX_3$ PNCs displays poor phase stability under high humid (>60%) conditions. We have tabulated a few possible suggestions as Table I to overcome this issue.

Surface Chemistry

In contrast to their bulk counterparts, colloidal halide PNCs have a very high surface-to-volume ratio, which highlights the importance of the NC surfaces in controlling their optoelectronic properties and environmental stability. For instance, in the case of a 10 nm $CsPbBr_3$ NC, nearly 20% of the atoms are present on its surface. Therefore, a clear understanding of the surface chemistry or capping ligand-surface characteristics of halide PNCs is vital for achieving higher optoelectronic device efficiencies. A highlight of the NC surface-passivating ligand property of the halide PNCs is that they can retain their bright emission properties despite the removal or displacement of a substantial number of passivating ligands, as predicted by Infante with their electronic structure calculations on $CsPbBr_3$ NCs.[45] However, the purification (postsynthetic washing procedure of the NCs)-induced PL QY loss can be attributed to aggregation of the NCs, which leads to a loss of quantum confinement, and hence emission intensity, rather than the formation of new surface defects ensured by the defect tolerance nature of halide PNCs.[45]

A conventional hot-injection synthesis of cubic-shaped $CsPbBr_3$ NCs has been predicted to result in NCs whose surfaces terminate with (001) and (110) crystal planes (facets).[45] A high-resolution TEM study of $CsPbBr_3$ NCs verified the (001) and (110) facet termination of their surfaces.[46] Consequently, based on the information about the nature of the NC surface and the particle morphology, two types of surfaces can be possible for $CsPbBr_3$ NCs: CsBr- and $PbBr_2$-terminated surfaces. Ravi et al. deduced the elemental stoichiometry of $CsPbBr_3$ NCs as a function of their thickness (from surface to bulk portions) using variable-energy X-ray photoelectron spectroscopy (XPS), as shown in Fig. 2a.[46] They found that Br:Cs was close to 5 on the NC surface, and the value decreased to ~3 when the bulk regime of the PNCs was probed. These results suggest that excess Br was present on the $CsPbBr_3$ NC surface. They also determined that Cs:Pb ratio was 1 on the surface as well as in the bulk portion of the NCs. Because Br:Pb is >3:1 but not <3:1 (which is the case of $PbBr_2$-termination) the NCs are expected to have a CsBr-terminated surface, where a few Cs sites are occupied by alkylammonium cations. Surface-sensitive ^{133}Cs solid-state NMR spectroscopy further verified that the surface of $CsPbBr_3$ NCs terminated with Cs and Br, but not with Pb and Br (Fig. 2b).[47] An additional ^{133}Cs NMR signal confirmed the presence of Cs ions on the NC surface. Similarly, excess Cs and I are present on the surface of $CsPbI_3$ NCs, as revealed by high-angle annular dark-field scanning transmission electron microscopy (HAADF-STEM) with atomic resolution.[48] The modeling of the $CsPbX_3$ NC surface by Infante and coworkers revealed that PbX_2-termination would require approximately 2.5 times denser ligand packing, which leads to steric hindrance, and which can destabilize the perovskite structure by disturbing the octahedral environment around Pb^{2+} ions.[49]

Long-chain primary alkylammonium and long-chain carboxylate ligands are the conventional surface-passivating ligands employed for $CsPbX_3$ NCs. These surface-bound ligands dynamically exchange with free ligands present in the solution, as realized with the help of proton NMR.[52] The highly dynamic nature of these capping ligands (Fig. 2c) results in their loss during the purification procedures of $CsPbX_3$ NCs, which leads to poor stability or colloidal stability of the NCs.[50] An interesting class of capping ligands are zwitterionic ligands that contain both cation- and anion-binding functional groups (exhibiting a chelation effect). Kovalenko et al. demonstrated the mode of binding of a few commercially available zwitterionic ligands such as sulfobetaine; the cationic quaternary ammonium and the anionic sulfonate groups of it occupy surface Cs-site vacancies (similar to oleylammonium ions) and bind to the surface of Pb (Fig. 2d).[51] Zwitterionic ligands ensure the production of highly pure NCs with PL QYs >90% after a few rounds of precipitation/redispersion, along with the formation of monodisperse $CsPbX_3$ NCs. Zeng et al. proposed a *Br-equivalent ligand* approach; benzenesulfonic acid strongly binds to exposed Pb sites while eliminating bromide vacancies.[53] Such binding not only ensures high PL QYs (>90%) but also preserves the structural and photophysical properties, even after many purification/redispersing cycles.

The binding strength of the capping ligands also affects the phase stability of halide PNCs. In another report, Dutta et al. realized that alkylammonium ions passivate the surface firmly and prevent phase instability of $CsPbI_3$ NCs when synthesized at a very high temperature (260 °C).[54] The stronger binding (in a nondynamic nature) of the alkylammonium ions to the NC surface prevents lead iodide octahedral titling, which acts as one of the NC degradation pathways. Bakr et al. demonstrated a postsynthetic treatment of oleic acid-capped $CsPbI_3$ NCs with a bidentate ligand (2,2-iminodibenzoic acid; IDA).[40] The IDA-treated $CsPbI_3$ NC film remained in the photoactive black phase even after 40 d of storage, whereas the untreated NC film was converted into PbI_2. The IDA ligands through two carboxyl groups bind strongly to the surface of $CsPbI_3$ NCs, resulting in the reduction of surface trap states and injection of extra electrons into the $CsPbI_3$ NCs. Postsynthetic surface treatments have also been employed to address colloidal stability issues. The addition (simultaneous cationic and anionic ligand exchange) of didodecyldimethylammonium bromide (DDAB quaternary ammonium salt) improved the colloidal stability and 100% PL QY.[49] The stronger binding and efficient passivation of DDAB ligands imparts NCs with a lower surface trap density by the removal of bromine vacancies. Table II summarizes the role of various ligands discussed here. A

Table I. Possible solutions to improve the phase stability of $CsPbX_3$ PNCs under high humid conditions.

Major challenge	Approach	Probable outcome/rationality
The phase stability of CsPbX3 NCs still remains poor under high moisture (>60% RH)	Tuning A-site cations	Doping of new organic (larger or smaller) cations may improve their stability by altering their structural parameters
	Simultaneous tuning of B- and X-site ions	Simultaneous tuning may lead to enhanced stability and desired band gaps
	Reducing surface energy by proper surface passivation	More effective passivation strategies are desired. Also, atomic level picture of surface passivation needs to be studied/developed.

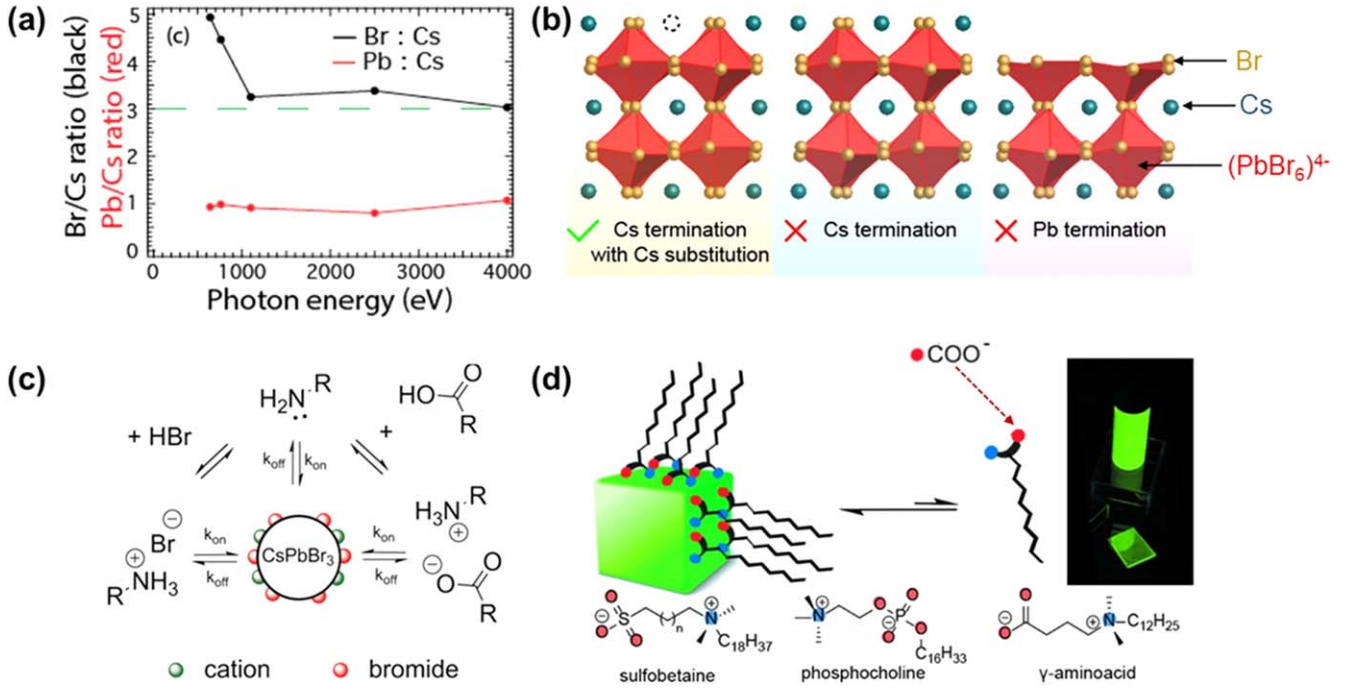

Figure 2. (a) Variation of Br:Cs and Pb:Cs as a function of photon energy (probing the ratios from surface to the bulk of the NCs by XPS).[46] (b) The surface of $CsPbBr_3$ NCs terminates with Cs and Br (and not with $PbBr_2$) and some of the Cs^+ ions are replaced by alkylammonium ligands, as demonstrated by[133] Cs solid-state NMR spectroscopy.[47] (c) Depiction of the dynamic surface stabilization by alkylammonium bromide, alkylammonium oleate and alkylamine.[50] (d) Zwitterionic molecule binding to produce highly stable and bright emitting $CsPbBr_3$ NCs.[51]

few suggestions to improve the performance of capping ligands in the viewpoint of better optoelectronic device performance based on $CsPbX_3$ PNCs are summarized on Table III.

Encapsulating Strategies for Improving Stability of PNCs and WLEDs

Inorganic materials as encapsulating matrices.—Several inorganic materials such as oxides (SiO_2, TiO_2, Al_2O_3, ZnO, and ZrO_2), salts ($NaNO_3$), and metal halides (MHs) (KCl, KBr, $ZnBr_2$, $InBr_3$, $CuBr_2$, ZnI_2, and $PbBr_2$) are transparent, mechanically robust, and airtight, with very low solid-state ion diffusion rates of ions, which are effective encapsulation layers to protect PNCs from external environmental conditions.[14] Among these materials, oxides (SiO_2, Al_2O_3, and TiO_2) and combination of SiO_2/Al_2O_3 may provide better stability against environmental and chemical factors and minimize pinhole defects, in addition to preserving the luminescence properties of PNCs.[14,55–58] These oxides are formed by a hydrolysis reaction by using precursors such as tetraethoxysilane (TEOS),[59–62] (3-aminopropyl) triethoxysilane (APTES),[61–68] tetramethoxysilane (TMOS),[16,60,67,69–71] methacryloxy propyl trimethoxyl silane (MPS),[60] trimethoxy(octadecyl)silane (TMODS),[61,68,72] 1H,1H,2H,2H-perfluorodecyltriethoxysilane (PFDTES),[59] di-sec-butoxyaluminoxytriethoxysilane (DBATES),[56] tridecafluoroalkyl-1,1,2,2-tetrahydrooctyltrichlorosilane (FAS),[73] polyhedral oligomeric silsesquioxanes (POSS),[74] titanium butoxide (TBOT),[14,75] tantalum (V) ethoxide (TTEO),[14] perhydropolysilazane (PHPS),[76] and others.[14] The volume of water and hydrolysis parameters of precursors, such as a higher water consumption rate and a lower water content, benefit encapsulation.[14] The most frequently reported precursor for SiO_2 is (3-aminopropyl) triethoxysilane (APTES), owing to its high hydrolysis rate.[57–64] The luminescence properties of @SiO_2 composites can be improved by tuning the Pb:Si molar ratio, demonstrating the significance of the precursor quantity and hydrolysis rate.[14,62,69] Furthermore, APTES has three benefits.[61–68] First, APTES acts as a capping agent for inorganic PNCs, is useful for dissolving PbX_2 and stabilizing PNCs,[61–68] and as a precursor for the SiO_2 passivating layer. Second, the amino group from APTES can effectively encapsulate the PNC surface to preserve its original high PL QY.[61–68] Third, the three silyl ether groups can be hydrolyzed to form a cross-linked matrix to cover the PNCs.[61–68] For instance, Sun et al. reported that PNCs-APTES is a one-pot encapsulation of large quantities of PNCs with a SiO_2 layer, which enhanced their environmental stability.[65] The prepared green $CsPbBr_3$ PNCs and red $CsPb(Br/I)_3$ PNCs/SiO_2 composites exhibited PL QYs of 78% and 68%, respectively, compared to their colloidal PNC solutions, which were 85% and 88%, respectively.[65] The PNCs/SiO_2 composites were stored for three months in air at room temperature. The PL QY of the $CsPbBr_3$ PNCs/SiO_2 composites showed nearly no variation over three months, whereas a 5% drop over three months was reported for $CsPb(Br/I)_3$ PNCs/SiO_2. However, the decrease in PL intensity with increasing temperature indicates the thermal instability of PNCs/silica at higher temperatures. The prepared $CsPbBr_3$ PNCs/SiO_2 composites demonstrated good stability in air, and anion-exchange reactions were not detected between different PNCs, which are favorable for fabricating WLED devices. The WLED devices fabricated with the green and red PNCs/SiO_2 composites with a blue LED chip, display Commission Internationale de l'Eclairage (CIE) color coordinates of (0.33, 0.33) and a luminous efficacy (LE) of 61.2 lm W^-.[65] The power efficiency might be further strengthened by an increase in the chip efficiency, improving the structure of the remote configuration, and decreasing the scattering of light. The PL emission spectrum of the WLED was evaluated at an operating current of 20 mA over 10 h. The performance of the device could be further strengthened by increasing the PL QY and increasing the crystallinity and morphology to reduce ion migration.[65]

Weiwei Chen et al. fabricated silica (APTES)-wrapped Mn-doped $CsPbCl_3$ PNCs for WLEDs.[66] The Mn-doped $CsPbCl_3$ PNCs/SiO_2 composite exhibited a PL QY of 55.4%. The SiO_2-passivated $CsPbMnCl_3$ PNC composites could be protected from temperature, moisture, and anion exchange.[66] WLEDs were prepared using a mixture of green $CsPbBr_3$ PNCs and orange-red Mn-doped $CsPbCl_3$@SiO_2 composites. The fabricated white LED displays an LE of 77.59 lm W^{-1}, a color rendering index (CRI) of

Table II. Summary of roles of different capping ligands.

Capping ligand	Advantages	Disadvantages
Long-chain primary alkylammonium and carboxylates[52]	Good PNC surface passivation	Loss of ligands during NC purification, thereby leads to poor NC colloidal stability
Zwitterions[51]	Contain both cation- and anion-binding functional groups. Ensure the production of highly pure PNCs	
2,2-iminodibenzoic acid	The two carboxyl groups bind strongly to PNC surface. Injection of extra electrons into PNCs.	
Didodecyldimethylammonium bromide	Stronger binding and efficient NC surface passivation.	

Table III. Possible solutions to overcome the capping ligand challenges for achieving higher optoelectronic device efficiencies.

Challenges	Solution
Poor charge transport in the devices due to commonly used long chain capping ligands	Replacement with short chain ligands
	Introducing capping ligands possessing extra charge
	Using short inorganic capping ligands for better passivation and charge transport
Possible segregation of mobile capping ligands on the PNC surface under various operating conditions	Development of more chemically stable capping ligands

82, and a color temperature (CCT) of 3950 K.[66] Furthermore, the electroluminescence (EL) spectrum did not change even after 24 h of operation. These results suggest that the SiO_2-encapsulated Mn-doped $CsPbCl_3$ PNC composites will prove to be a prospective candidate for WLEDs. Liang et al. promoted SiO_2-passivated PNCs (SP-PNCs) by in situ hydrolysis of the surface ligands of APTES.[63] The resultant SP-PNCs possessed a PL QY of 80%. Furthermore, the prepared SP-PNCs were incorporated into polystyrene microspheres (PMs) to increase their long-term storage stability. The initial PL QY of the as-prepared SPPNC-PM composite was approximately 65%. The PL QYs of SP-PNCs and SP-PNCs-PMs after 60 d storage in air were retained at 50% and 20%, respectively.[63] These results showed that the PMs acted as an efficient barrier to protect SP-PNCs from external environmental conditions.[63] Overall, the inorganic passivation layers demonstrated better stability against light and oxygen. However, PNCs inevitably suffer at high temperatures because the heat can transfer via the inorganic layer toward PNCs, thus leading to poor thermal stability.[14,77] In addition, several issues remain, which are as follows.[62] (1) The hydrolysis of organosilane introduces polar solvents into the $CsPbX_3$PNCs@SiO_2 matrix during the synthesis process, which affects the luminescence properties of PNCs[62]; (2) weak interaction between the $CsPbX_3$ PNCs@SiO_2 layers generates phase separation[62]; and (3) the destruction of the monodispersity of $CsPbX_3$ PNCs in SiO_2 layers leads to spontaneous grain aggregation, which increases the number of surface defects. These issues affect the crystal structure and luminescence properties of $CsPbX_3$ PNCs.[62] To resolve these problems, dual-encapsulation strategies such as passivation of $CsPbX_3$ PNCs with dual-shell hollow SiO_2,[62] $CsPbBr_3$@CA-SiO_2,[78] $CsPbX_3$PNCs@SiO_2/poly(methylmethacrylate) (PMMA),[71] $CsPbBr_3$PNCs/$FSiO_2$/PPDMS,[59] DDAB-$CsPbBr_3$ PNCs@SiO_2,[69] superhydrophobic nanocomposites,[72] and others have been used to protect PNCs under various environmental conditions.[62]

Zhou et al. proposed an in situ encapsulating approach to form superhydrophobic nanocomposites ($CsPbBr_3$PNCs@SSiP) by integrating $CsPbBr_3$ PNCs into organosilica nanoparticles (Fig. 3a),[72] which reduced the luminescence properties and enhanced the environmental stability (Fig. 3a). The PL QY of the prepared $CsPbBr_3$ PNCs@SSiP was over 50%. The $CsPbBr_3$PNCs@SSiP nanocomposites maintained >75% of their original PL intensity after 10 d of immersion in water, whereas pristine $CsPbBr_3$ PNCs demonstrated complete luminescence quenching in 1 h[68]. The PL intensity was 90% for the $CsPbBr_3$ PNCs@SSiP nanocomposites even after 90 d of exposure to air, whereas the PL intensity of pristine $CsPbBr_3$ PNCs was reduced to 20% within 10 d. The $CsPbBr_3$PNCs@SSiP nanocomposites can preserve >80% of their original PL intensity, even after 120 h of UV irradiation, whereas pristine $CsPbBr_3$ PNCs demonstrated obvious quenching in 24 h.[72] The PL intensity of the $CsPbBr_3$ PNCs decreased to <20% over 10 d, whereas the PL intensity of the PNC@SSiP nanocomposites dropped only 10% of its original value even after 90 d (Fig. 3b).[72] The PL intensity of PNC@SSiP decreased significantly at 150 °C. Surprisingly, the PL intensity of PNC@SSiP after heating at 150 °C was restored to 20 °C. These results suggest that the prepared $CsPbBr_3$ PNCs@SSiP demonstrated good stability in water, as well as improved thermal stability and photostability.[72] The fabricated PNC@SSiP nanocomposites showed high stabilities and high PL QYs that could be used in WLEDs. The WLED was manufactured by depositing PNC@SSiP nanocomposites with green emission and YAG phosphor with red emission onto a 460 nm GaN LED chip. The fabricated WLED shows CIE color coordinates of ($x = 0.31$, $y = 0.34$), CRI of 54.3, and LE of 22.6 lm W^{-1} under an operating current of 20 mA.[72] Tu et al. reported a novel dual-encapsulation approach using a combination of fluorinated silica ($FSiO_2$) and thermally insulated porous polydimethylsiloxane (PPDMS) to enhance the stability of PNCs.[59] The PL intensities of the $CsPbBr_3$ PNCs, $CsPbBr_3$ PNCs/$FSiO_2$, and $CsPbBr_3$PNCs/$FSiO_2$/PPDMS composites decreased to 7.4%, 29.8%, and 50.0% of their initial values, respectively, as the temperature increased from 30 to 90 °C (Fig. 3d).[59] A temperature-dependent PL study indicated that the $CsPbBr_3$ NCs/$FSiO_2$/PPDMS composite exhibited better thermal stability than the others. The higher thermal stability of the $CsPbBr_3$ NCs/$FSiO_2$/PPDMS composite is attributed to its porous structure, low thermal conductivity, and good thermal insulation properties of PPDMS.[59]

The $CsPbBr_3$ PNCs/$FSiO_2$/PPDMS composites showed robust green luminescence after floating on the water surface, even after 5 months (inset Fig. 3e).[59] The relative PL of $CsPbBr_3$ NCs/$FSiO_2$ was reduced to 96.5% even after storage for 90 d in air, whereas the PL intensity of the $CsPbBr_3$ PNCs/$FSiO_2$/PPDMS composite was nearly constant even after storage for 90 d (Fig. 3e).[59] The PL intensities of the $CsPbBr_3$ NCs/$FSiO_2$ and $CsPbBr_3$ NCs/$FSiO_2$/PPDMS composites remained above 90% and 96% of their initial values under continuous UV light irradiation for 50 h, respectively. Two $CsPbBr_3$ NCs/$FSiO_2$/PPDMS composite films and $CsPbBr_{1.8}Cl_{1.2}$ PNCs/$FSiO_2$/PPDMS composite films were kept together to further evaluate the anion-exchange stability. The anion exchange between the $CsPbBr_3$ NCs/$FSiO_2$/PPDMS composite films and $CsPbBr_{1.8}Cl_{1.2}$ NCs/$FSiO_2$/PPDMS composite films was observed after 30 h, suggesting that the $FSiO_2$ and PPDMS layers could effectively restrict the anion exchange.[59] Owing to the superhydrophobic and thermal insulation layers, the luminescence properties of dually encapsulated $CsPbBr_3$ PNCs are stable under external environmental conditions for 3 m. Considering these attractive stability properties, $CsPbBr_3$ NCs/$FSiO_2$/PPDMS composites have been utilized to fabricate WLEDs. A WLED device was constructed by blending prepared green $CsPbBr_3$ NCs/$FSiO_2$ powders, blue $BaMgAl_{10}O_{17}$:Eu powders, and red (Sr, Ca) $AlSiN_3$:Eu powders with silicone resin thoroughly, and then coating the mixture on a 400 nm UV chip (Fig. 3f). The WLED shone with a bright white light (Fig. 3f).[59] The fabricated WLED showed the CIE chromaticity coordinates of (0.33, 0.33), LE of 10.7 lm W^{-1}, CCT of 5235 K, and CRI of 52.9, at a driving current of 20 mA.[59] Varnakavi Naresh et al. reported that the dual passivation of blue-green-red-emitting $CsPbX_3$ (X = Cl/Br, Br, and Br/I) PNCs/SiO_2/PMMA displays enhanced stability (thermal, moisture, and photostability).[69] The dual-passivated $CsPbX_3$ (X = Cl/Br, Br, and Br/I) PNC SiO_2/PMMA composite films exhibited PL QYs of blue, green, and red emission of 37%, 86%, and 71%, respectively.[71] The NCC-encapsulated SiO_2/PMMA composite films were incorporated into the UV LED chip to assemble WLEDs. The designed WLED showed CIE coordinates (0.349, 0.350), an LE of 39.2%, and a CRI of 84.7.[71] These results show that $CsPbX_3$ (X = Cl/Br, Br, and Br/I) PNCs@SiO_2/PMMA composite films can be used as efficient UV to visible color conversion materials such as WLEDs and backlighting. The stability of the luminescence properties and white PLED performance of various SiO_2 passivated $CsPbX_3$ NCs/NCs are summarized in Tables III and IV.

Inorganic glass matrices.—Inorganic glass matrices have been sought-after owing to their outstanding mechanical, thermal, and chemical stabilities.[13,85,86] It has been reported that PNCs/NCs embedded in a glass matrix avoid the agglomeration of PNCs, and the thermal stability and chemical stability are improved owing to the superior thermal resistance of the glass.[13,85,86] Therefore, PNCs@glasses have several advantages, such as tunable emission, narrow luminous range, good photo/thermal stability, and water resistance.[13] $CsPbX_3$ PNCs/NCs have been embedded successfully in various glass matrices such as borosilicate,[86,87,91,113–117] phosphosilicate,[88,89] TeO_2-based glass,[90] germanate glass,[13] and Zn-P-B-Sb-based oxides for improving the operational stability of white PLEDs.[13] PNCs embedded in a glass matrix were prepared by traditional melting-quenching followed by a heat treatment process (Fig. 4a)[91] and in situ nanocrystallization processes (Fig. 4b).[90] The thickness of the PNC layer,[115] heat treatment conditions,[77,85,91,115] raw components of the glass matrix,[77,88] phase transition,[86] molar ratio of the initial precursor for $CsPbX_3$,[86] and chemical composition of PNCs affects the PL properties and stability of WLEDs.[13,86,88,91]

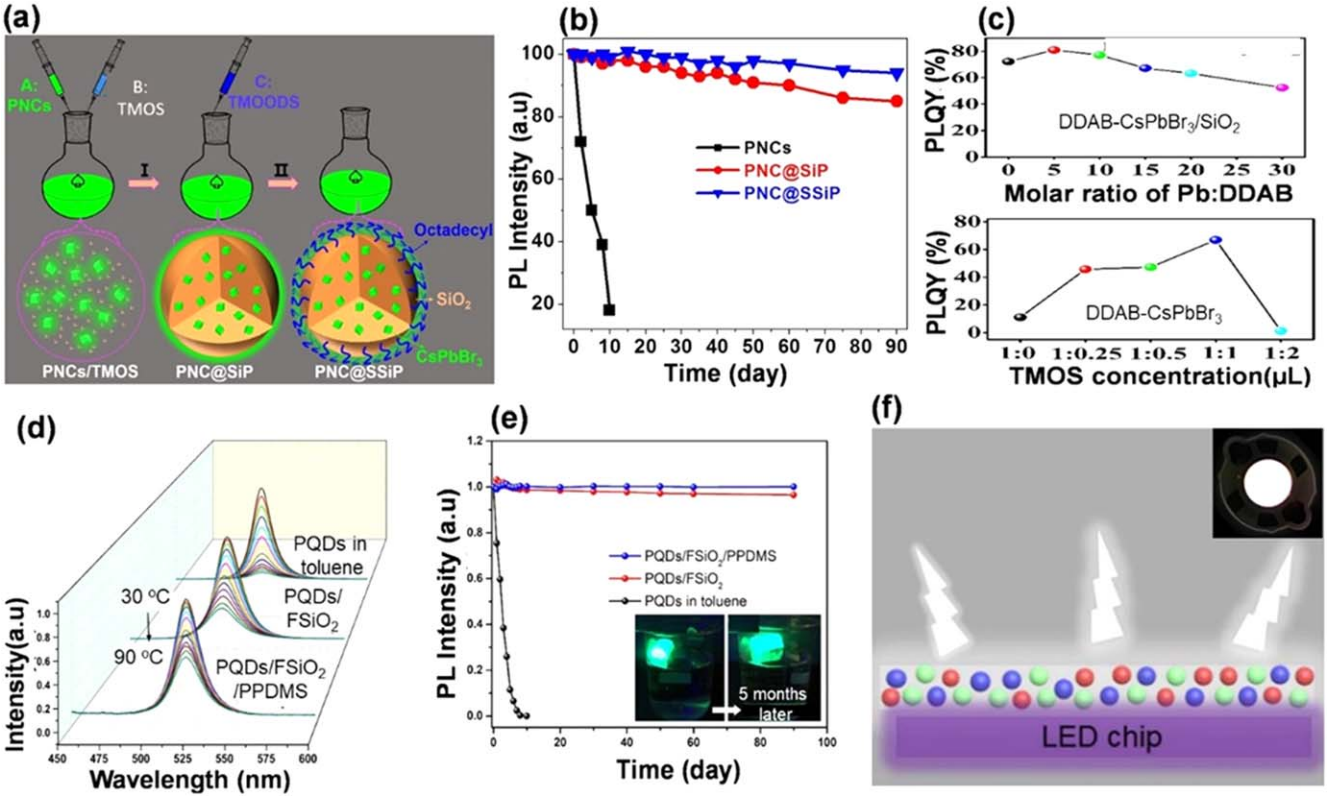

Figure 3. (a) Synthesis of $CsPbBr_3$PNCs@super-hydrophobic nanocomposites (PNCs@SSiP).[72] (b) Relative fluorescence intensity of the PNCs@SSiP nanocomposites storing under atmosphere over time.[72] (c) PL QY of DDAB-$CsPbBr_3$ PNCs with different molar ratios of Pb:DDAB and TMOS concentration. (d) PL spectra of $CsPbBr_3$ NCs in toluene, $CsPbBr_3$NCs/$FSiO_2$ powders, and $CsPbBr_3$ NCs/$FSiO_2$/PPDMS composite as a function of temperature from 30 to 90 °C.[59] (e) PL intensity of $CsPbBr_3$ NCs in toluene, $CsPbBr_3$ NCs/$FSiO_2$ powders, and $CsPbBr_3$ NCs/$FSiO_2$/PPDMS composite as a function of time with RH of 60 ± 5% and temperature of 25 ± 2 °C.[59] (f) Schematic diagram of WLED structures (inset: photograph of WLED fabricated by the desorbed $CsPbBr_3$ NCs/$FSiO_2$ particles operated at 20 mA).[59]

Zhang et al. reported Rb^+-doped $CsPbBr_3$ PNCs stabilized in borosilicate glass via traditional melting-quenching followed by a heat treatment process (Fig. 4a).[91] Borosilicate glass has a high surface flatness, high thermal shock resistance, high surface hardness, good acid and alkali resistance, and good hydrolysis resistance.[13] The $CsPbBr_3$ PNCs/glass matrix exhibited good stability under different atmospheric, light, water, and heat conditions.[91] The time-dependent relative PL intensities of colloidal Rb^+-$CsPbBr_3$ NCs, Rb^+-$CsPbBr_3$ NCs/SiO_2, and Rb^+-$CsPbBr_3$ NCs/glass matrix were measured under an air atmosphere for 20 days of storage at regular time intervals (Fig. 4c).[91] The relative PL intensities of 18%, 55.3% and 97.2% are maintained for Rb^+-$CsPbBr_3$ NCs, Rb^+-$CsPbBr_3$ NCs/SiO_2, and Rb^+-$CsPbBr_3$ NCs/glass matrix after 20 days storage in air, respectively. The Rb^+-$CsPbBr_3$ NC/glass matrix retained good green fluorescence emission even after 10 days of complete immersion in water. All the findings suggest that the dense network of the glass matrix partially impeded the erosion of external environmental factors on the PNCs. The relative PL intensities of 5.08%, 11.73%, and 35.5% were retained for Rb^+-$CsPbBr_3$ NCs, Rb^+-$CsPbBr_3$ NCs/SiO_2, and Rb^+-$CsPbBr_3$ NCs/glass matrix, respectively, when the temperature increased to 105 °C (Fig. 4d).[91] The relative PL intensity of the Rb^+-$CsPbBr_3$ NC/glass matrix did not change even after continuous exposure to a UV lamp for 192 h, demonstrating the excellent photostability of the PNC glass. All these stability findings suggest that PNC glasses have a huge potential for WLED applications. The WLED device comprises an InGaN chip matching a $CsPbBr_3$:0.4Rb NC glass coated with $CaAlSiN_3$: Eu^{2+} phosphor. The fabricated WLEDs display CIE chromaticity coordinates of (0.3275, 0.3303), CRI of 73.4, CCT of 5732 K, and LE of 24.60.[91] Zou et al. studied the effects of raw components of the borosilicate glass matrix and its heat treatment conditions on the crystallization process, the molar ratio of initial precursors for $CsPbX_3$, the chemical composition of PNCs, and the role of the Cs_4PbBr_6 phase on the $CsPbBr_3$/Cs_4PbBr_6 composite-based PL properties and stability of W LEDs.[85,86] Heat treatment conditions (temperature and time) play a key role in obtaining the PL QY of $CsPbBr_3$/Cs_4PbBr_6 composites in glass.[86] The maximum PL QY of 61.2% was obtained for the $CsPbBr_3$/Cs_4PbBr_6 composite PNCs in glass heat-treated at 430 °C for 3 h.[85] When the $CsPbBr_3$/Cs_4PbBr_6 composite PNCs in glass was treated at 85 °C and RH 85% for 110 h, the PL intensity retained 80% of its initial value.[85] The PL intensity decreased to 55% of the initial value under the xenon lamp exposure for 110 h. The WLED devices made of the $CsPbBr_3$/Cs4$PbBr_6$ composite in glass as a green phosphor were blended with the red phosphor K_2GeF_6:Mn^{4+} on a commercial blue LED. The WLED exhibited an LE of 78.98 lm W^{-1} and CIE coordinates of (0.3195, 0.3262) at a constant driving current of 90 mA.[85] The impact of the raw components and melting conditions on the crystallization process, phase transition, and crystal growth of $CsPbBr_3$/Cs_4PbBr_6 NCs in a borosilicate glass matrix and their influence on thermal stability, photostability, and water resistance stability have been addressed previously.[86] The maximum PL QY of ~58% $CsPbBr_3$/Cs_4PbBr_6 NCs @glass was achieved with the optimum $PbBr_2$/Cs_2CO_3 molar ratio (6:1) in the raw materials.[86] The relative PL intensity of $CsPbBr_3$/Cs_4PbBr_6 PNCs@glass was retained at 92% and 80% of the initial values after heating/cooling cycles at 150 °C and 200 °C, respectively. The PL intensity remained at 80% of the original values of the $CsPbBr_3$/Cs_4PbBr_6 composite PNCs in glass treated at 85 °C and 85% RH for 70 h.[86] The PL intensity dropped to 50% of the initial value after exposure to the xenon lamp for 70 h. Two factors can induce a decline in the PL intensity of NCs@glass by xenon

Table IV. Comparison of the stability of PL properties of $CsPbX_3$ NCs coated with different materials.

PNCs	Passivating materials or the strategy	Stability (remaining PL)						References.
		PL QY (%)	In air	In water	photostability	Ion exchange	Thermal stability	
				Metal ions doping				
$CsPbBr_3$	Zn^{2+} ion doping	91.3	168 h/92.1%	N/A	N/A	N/A	77 °C/40%	79
$CsPbCl_3$	Sm3 + ion doping	85	42 d/30%	N/A	N/A	N/A	N/A	80
$CsPbBr_3$	Sn^{2+} ion doping	82.77	N/A	N/A	N/A	N/A	80 °C, 105 min/93%	81
$CsPbCl_3$	Mn2 + ion doping	52	30 months/ 100%	N/A	N/A	N/A	N/A	82
$CsPbBr_{2.2}Cl_{0.8}$	$Tm^{3+/}Mn^{2+}$ ion doping	54	60 h/100%	N/A	N/A	N/A	80 °C, 24 h/90%	83
				Oxide's layer				
$CsPbBr_3$	$FSiO_2$/PPDMS	64	3 months/ 100%	5 months/ 86%	50 h/96%	30 h $N^{-1}o^{-1}$ ex-change	90 °C, 36 min/50.0%	59
$CsPb(Br_{)3}$	SiO_2 (APTES)	78	3months/ 100%	N/A	N/A	N/A	N/A	65
$CsPb(Br/I_{)3}$	SiO_2 (APTES)	68	3 months/ 95%	N/A	N/A	N/A	N/A	65
Mn-Doped $CsPbCl_3$	SiO_2 (APTES)	55.4	15 d/69%	N/A	N/A	N/A	60 °C/100%, 100 °C/ 61.70%,	66
$CsPbBr_3$	SiO_2 (APTES)/PS	80	2 months/ 77%	N/A	N/A	N/A	N/A	63
$CsPbBr_3$	superhydrophobic SiO_2	50	3 months/ 90%	20 d/60%	120 h/80%	N/A	150 °C, 50%	72
$CsPbBr_3$	SiO_2/Al_2O_3		N/A	2 h/ ~ 96%	40 h/80%	N/A	N/A	72
DDAB-$CsPbBr_3$	SiO_2	80	N/A	40 min/	N/A	N/A	N/A	70
$CsPbBr_3$	SiO_2		N/A	N/A	30 h/83.5%	N/A	N/A	60
$CsPbX_3$	CA-SiO_2	76	N/A	60 d/95%	156 h/81%	N/A	120°C/82%	68
$CsPbBr_3$	CA-SiO_2	76	N/A	8 d/59%	100 h/82%	N/A	N/A	68
$CsPbBr_3$	dual-shell SiO_2	89	N/A	N/A	72 h/ 89%	N/A	100 °C/65%	62
$CsPb(Cl_{0.5}/Br_{0.5})_3$	SiO_2/PMMA	37	NA	25 d/76.2%	25 d/67.36%	NA	100 °C, 54.61%	71
$CsPbBr_3$	SiO_2/PMMA	86	NA	25 d/86.5%	25 d/83.48%	NA	100 °C, 69.88%	71
$CsPb(Br_{0.4}/I_{0.6})_3$	SiO_2/PMMA	71	NA	25 d/77.5%	25 d/79.18%	NA	100 °C, 58.34%	71
Mn-doped $CsPbCl_3$	SiO_2/Al_2O_3	49	NA	NA	7 d/92%	NA	NA	57
$CsPbBr_3$	Mica	38.5	N/A	N/A	7 d/88%	N/A	N/A	84
				Glass matrix				
$CsPbBr_3/Cs_4PbBr_6$	borosilicate glass	61.2	N/A	N/A	110 h/45%	N/A	85 °C, 110 h/80%	85
$CsPbBr_3/Cs_4PbBr_6$	borosilicate glass	58	N/A	70 h/98%	70 h/50%	N/A	85 °C, 70 h/80%	86
Gd^{3+} -CsPbBrI	borosilicate glass	37	N/A	60 d/100%	40 min/100%	N/A	130 °C/80%	87
$CsPbX_3$	Phosphosilicate glass	15.6	N/A	N/A	N/A	N/A	300 °C,2 h/15.6%	88
$CsPb(Br/I)_3$	P–Si–Zn glass		500 h/95.9%	960 h/90%	960 h/90%	N/A	180 °C, 75%	89
$CsPbBr_3$	TeO_2 glass matrix	70	45 d/60%	120 h/90%	N/A	N/A	100–200 °C, 60%–70%	90
Rb^{+}- $CsPbBr_3$	borosilicate glass		20 d/97.2%	10 d/100%	192 h/100%	N/A	105 °C, / 35.5%	91
				Porous/Metal–Organic Frames (MOFs)				
$CsPbBr_3$	ZIF-8	72	75 d/80%	NA	72 h/ 80%	30 min $N^{-1}o^{-1}$ ex-change	NA	92
$CsPbBr_3$	MOF-5	54	60 d/79.2%	NA	80 h/71.4%	30 min $N^{-1}o^{-1}$ ex-change	80 °C,72.8%	93
$CsPbBr_3$	Uio-67	38.5	30 d/100%	N/A	N/A	N/A	N/A	94

Table IV. (Continued).

PNCs	Passivating materials or the strategy	Stability (remaining PL)						References.
		PL QY (%)	In air	In water	photostability	Ion exchange	Thermal stability	
$CsPbBr_3$	LTA zeolite	66	17 months/ 100%	554 d/78%	20 d/100%	No exchange	60 °C,57%	95
$CsPbBr_3$	Zeolites-Y		N/A	N/A	N/A	N/A	120 °C/ ∼ 20%	17
$CsPbBrI_2$	Zeolite/PMMA	53.9	2 months/ 78%	20 d/94.7%	N/A	N/A	N/A	96
$CsPbBr_3$/POSS	POSS	61	N/A	Polymer Coating Over 10 weeks	N/A	5 min $N^{-1}o^{-1}$ exchange	N/A	74
$CsPbBr_3$/TDPA	TDPA	68	N/A	300 min/ 75%	N/A	N/A	100 °C, 59%	97
$CsPbX_3$/SBS	SBS		N/A	10 min/ 100%	N/A	N/A	N/A	98
$CsPbX_3$/PS	St		N/A	24 h/82%	N/A	N/A	N/A	99
$CsPbX_3$	PS sphere	68	N/A	1 month/ 30%	48 h/ ∼ 63%	24 h $N^{-1}o^{-1}$ exchange	N/A	100
$CsPb(I_{1-x}Br_x)_3$	PS	57	N/A	80 min/80%	N/A	N/A	N/A	101
$CsPbBr_3$	SEBS		N/A	110 d /94%	N/A	N/A	N/A	102
$CsPbBr_3$	UVR	64.0	60 d/88%	N/A	N/A	N/A	N/A	103
$CsPb(Br_{0.3}I_{0.7})_3$	UVR	59.4	60 d/70%	N/A	N/A	N/A	N/A	103
$CsPbBr_3$	PVDF	65	N/A	60 d/80%	N/A	N/A	N/A	104
$CsPbBr_3$	PMMA	65	N/A	30 d/50%	N/A	N/A	N/A	104
$CsPbBr_3$	PMMA	82	N/A	12 h/90%	N/A	N/A	N/A	105
$CsPbBr_3$	PMMA	82.7	N/A	15 d/53%	90 h/100%	N/A	80 °C, 24 h/81%	106
$CsPbBr_3$	PMAO	88.8	40 d/>90%	144 h/60%	144 h/94%	N/A	N/A	107
$CsPbBr_3$	CPB@SHFW	60	N/A	31 d/91%	N/A	N/A	N/A	108
$CsPbBr_3$	CNCs-$CsPbBr_3$@PVDF	N/A	N/A	50 d/80%	50 d/85%	N/A	N/A	109
$CsPbBr_3$	PDPEP-co-S	90	30 d/33%	3 d/87%	142 h/64%	N/A	N/A	110
$CsPbBr_3$	SBA-15-PMMA	80	N/A	30 d/91.1%	54 h/64%	N/A	80 °C, 16 h/60%	111
$CsPbBr_{1.5}I_{1.5}$	metal stearate	67	30 d/85%	N/A	N/A	24 h/No exchange	N/A	112

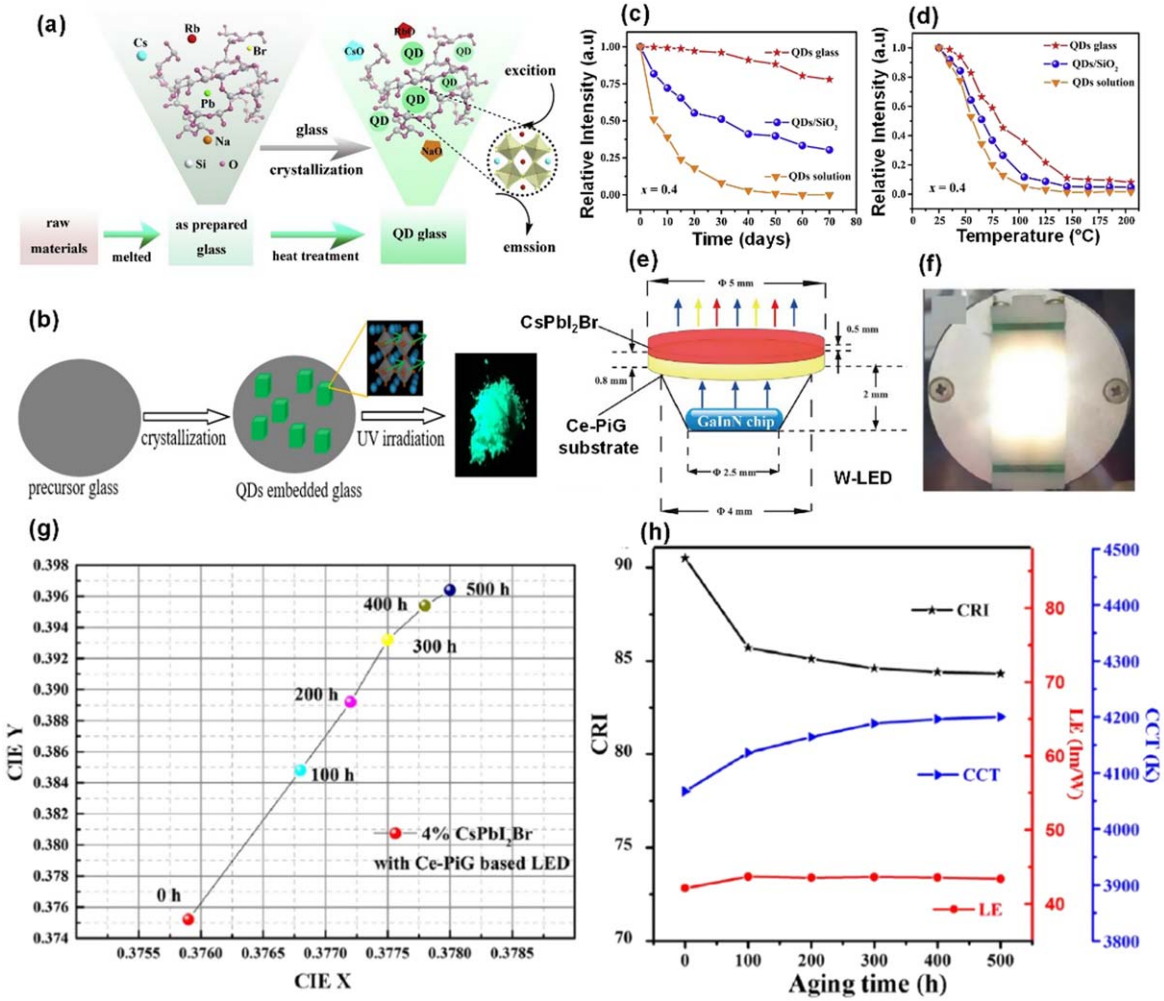

Figure 4. (a) Growth mechanism of the $CsPbBr_3$: xRb NCs—borosilicate glasses via glass crystallization via traditional melting-quenching followed by heat treatment process.[91] (b) In situ nanocrystallization of $CsPbBr_3$ NCs from TeO_2-based glass matrix and luminescent photograph of NCs@glass powder under irradiation of UV lamp (365 nm).[90] (c) Time- and (d) temperature-dependent PL intensity relative intensity of colloidal $CsPbBr_3$ PNCs, $CsPbBr_3$ PNCs/SiO_2 composite powders, and $CsPbBr_3$ PNCs/glass under air atmosphere, respectively.[91] (e) Schematic diagram of the WLED device model based on the Ce-PiG color converter with a $CsPbI_2Br$ concentration and a 0.5 mm thickness of ER.[118] (f) 7 wt% Ce-PiG and 4 wt% $CsPbI_2Br$-ER color converters.[118] Aging time-dependent (g) CIE coordinates and (h) CRI, CCT, and LE of the fabricated $CsPbI_2Br$-ER based WLED at 363 K.[118]

irradiation. First, xenon light exposure can lead to an increase in the local temperature. The decline in PL intensities was most probably associated with the surface decomposition of PNCs driven by OH^- at elevated temperatures. The OH^- groups present within the glasses may result in the decomposition of $CsPbBr_3$ nanocrystals during xenon irradiation, thus causing a decline in the PL intensity. The PL intensity of NCs@glass showed a small reduction (2%) after complete immersion in water for 70 h, while the colloidal $CsPbBr_3$ NCs were quickly decomposed, and their PL intensity decreased to ~5% after dipping in water for 2 h. These results suggest that the inorganic glass host can effectively shield PNCs from erosion of the external atmosphere and enhance their moisture resistance.[86] The WLED was manufactured using the as-synthesized green PNCs@glass powder and red $K_2SiF_6:Mn^{4+}$ phosphor on a blue LED chip surface. The fabricated WLED exhibits an LE of 25 lm W^{-1} and CIE coordinates of (0.3328, 0.3442) at 100 mA.[86] The major limitation of borosilicate glasses is that the high melting temperature (up to 1100 °C) required for preparing the glass matrix would lead to the evaporation of Br sources and decrease the amount of crystallized $CsPbBr_3$ phase in glass, leading to low luminescence and low PL QY.[13,85,86]

Yuan et al. developed an in situ nanocrystallization approach for $CsPbBr_3$ NCs in a low-melting TeO_2-based glass matrix (Fig. 4b).[90] The effect of crystallization conditions and crystallization phase on the PL QY of $CsPbBr_3$ PNCs @ TeO_2-glass was systematically investigated.[90] The cubic $CsPbBr_3$ NC@glass prepared under optimal crystallization conditions at 280 °C for 2 h showed a PL QY of 70 ± 2%, enhanced water resistance, and photo/thermal stability.[90] The photostability of $CsPbBr_3$ NCs-TeO_2-based glass was evaluated under the illumination of a UV lamp for 70 h. No substantial changes in PL intensity and full width at half maximum (FWHM) were observed, which might be due to dense glass-passivated $CsPbBr_3$ PNCs. PL spectra of NCs@glass were obtained with respect to the storage time in aqueous solutions. The relevant PL intensity retained ~90% of the initial value after 120 h of immersion in water, and approximately 60% of the PL intensity was retained after 45 days.[90] The PL intensity of NCs@glass was maintained at 60%–70% of the initial values after three heating/cooling cycles at 100, 150, and 200 °C, while that of colloidal $CsPbBr_3$ PNCs decreased to less than 10% under the same conditions. The results obtained from the temperature-dependent PL study indicate the crucial role of the TeO_2-based glass host in improving the thermal resistance of $CsPbBr_3$ PNCs.[90] WLED devices were constructed by combining commercial Eu^{2+}:$CaAlSiN_3$ red phosphor and green-emitting $CsPbBr_3$ NCs@glass powder with an InGaN blue chip to demonstrate their display applications. The designed WLED shows color coordinates of (0.33, 0.35), CRI of ~92, CCT of ~5600 K, and LE of

50–60 lm W^{-1}.[90] The intensity and position of the EL spectra did not exceed 30 days in air and the operation time was 48 h, confirming the excellent color stability of the designed NCs@glass-based WLEDs.[90] Yuan et al. successfully demonstrated the in situ nanocrystallization of $CsPbBr_3$ PNCs in TeO_2-based glass. However, the major limitations of TeO_2-based glass are its high cost owing to the use of expensive TeO_2 as the main glass matrix and the complexity of incorporating I^- into NCs to achieve multicolor emission.[13,90] Liu et al. reported that a $CsPbX_3$ epoxy resin (ER) composite integrated with $Y_3Al_5O_{12}:Ce^{3+}$ ($YAG:Ce^{3+}$) phosphor-in-glass (PiG) was manufactured using tape-casting techniques.[118] The $CsPbX_3$@ER composite possesses good thermal insulation and a high refractive index, which efficiently improves the stability of $CsPbX_3$ NCs.[118] A schematic drawing of the WLED is shown in Figs. 4e and 4f.[118] The Ce-PiG and $CsPbX_3$-ER composites exhibited improved stability and maintained the luminescent properties of the $CsPbX_3$NCs. The fabricated WLED demonstrated a CRI of 90.5, CCT of 4067 K, and LE of 42.12 lm W^{-1} under 20 mA driving current.[118] The fabricated $CsPbX_3$-ER composite demonstrates the viability of the present luminescent materials for WLED applications. $CsPbI_2Br$-ER composite light conversion showed a retention of 87.4% of its initial efficiency values after 500 h of accelerated aging at 85 °C/85% RH. The aging time-dependent CIE coordinates, CRI, CCT, and LE of the prepared WLED at 363 K are shown in Figs. 4g and 4h, respectively, illustrating that ER could deliver a high water/humidity resistance.[116] The stability of the luminescence properties and white PLED performance of $CsPbX_3$ NCs embedded in various glass matrices are summarized in Tables IV and V. As summarized in Table IV, the thermal stability of PNCs embedded in borosilicate glass is greater than those embedded in other materials such as tellurium-based glass matrix and Zn-P-B-Sb-based oxide glass matrix.[13] Notably, both borosilicate and phosphosilicate glass matrices are found to impart a very high thermal stability to PNCs.[85,88]

According to previous reports, surface passivation is crucial for high stability and high luminescence by embedding PNCs in a glass matrix.[13] PNCs embedded in a glass matrix demonstrated efficient and relatively stable PL properties. However, further optimization of the glass composition, crystallization conditions, and other factors is required to improve the PL QY of the PNCs embedded in the glass matrix.[13,85] In addition to PL QY, optical stability, such as photodarkening and unstable brightening of PNCs embedded in glass, need to be addressed for practical applications.[13,85]

Apart from above inorganic materials, hosts such as Cs_4PbX_6, $CsPb_2Br_5$, and NH_4Br have also been found to provide efficient encapsulation to $CsPbX_3$ PNCs. For instance, Bao and coworkers demonstrated that efficient EL properties can be achieved from $CsPbBr_3$ NCs encapsulated within Cs_4PbBr_6 matrix.[124] Similarly, $CsPb_2Br_5$ as a shell improves the stability of encapsulated $CsPbBr_3$ NCs against heat and humidity.[125] Dirin et al. found that alkali halide (such as KBr and NaBr)-coated PNCs have exhibited resistance towards polar solvents such as γ-butyrolactone and acetonitrile, and demonstrated high thermal stability, which are desirable for next-generation light emitting applications.[126] Similarly, $CsPbBr_3$@HNO_3 nanocomposite displays excellent thermal stability and water resistance compared to the bare PNCs.[127] The nanocomposite was synthesized via a low-cost and scalable method.

Encapsulation by metal–organic frameworks (MOFs).—MOFs are porous crystalline materials that exhibit tunable structures, large surface areas, and tailorable functionalities, and have attractive chemical and physical properties.[93,128,129] MOFs are built by the general assembly of inorganic metal nodes and multidentate organic linkers.[93,128,129] MOF materials are a good option for host matrices for various metallic nanoparticles, quantum dots, dye molecules, and others.[128,129] The role of MOF hosts is to isolate PNCs without aggregation and shield them from external environmental conditions.[128] For example, mesostructured zinc-based MOFs (MOF-5),[93] Zr-based MOFs (Uio-67),[94] zeolitic imidazolate framework-8 (ZIF-8),[92] LTA zeolite,[95] zeolite-Y,[123] zeoite/PMMA,[96] and others have been applied as host matrices to protect and encapsulate $CsPbX_3$ PNCs@PNCs.[128,129] The strong interaction between the ions of the NCs with the MOF atoms leads to the incorporation of PNCs into the pores of MOF. The screening criteria for MOFs for PNCs@MOF composites should consider the following three aspects: (1) stability, (2) porosity, and (3) synthesis conditions.[128] High-quality PNCs@MOF composites are essential for WLED applications. Recent research updates on PNCs or PNCs@MOF composites for WLED applications are systematically reviewed in the following section.

Rena et al. reported a new approach for improving the stability of $CsPbX_3$ PNCs to embed into the MOF-5 host (Fig. 5a).[93] MOF-5 acted as a dispersion medium to endow $CsPbX_3$ PNCs with enhanced thermal stability, photostability, long-term stability, and anion-exchange properties.[93] The PL QYs of $CsPbBr_3$ PNCs @MOF-5 and $CsPbBr_{0.6}I_{2.4}$ PNCs @MOF-5 composites were 52% and 56%, respectively, which are greater than those of the pristine $CsPbBr_3$ PNCs (∼34%) and $CsPbBr_{0.6}I_{2.4}$ PNCs (∼27%). The $CsPbBr_3$ PNCs @MOF-5 composite maintained 72.8% at 80 °C, 71.4% after UV lamp exposure for 80 h, and 79.2% of their initial PL intensity after 60 days in air (Fig. 5b). Owing to the enhanced stability of the $CsPbX_3$@MOF-5 composites, it can be used as a single down-conversion layer for WLEDs. The fabricated $CsPbX_3$ PNCs @MOF-5 based WLED shows the CIE of (0.375, 0.321), CCT of 3607 K, CRI of 83, and LE of 21.6 lm W^-.[93] The CIE color coordinate triangle of the $CsPbX_3$ PNCs @MOF-5 based W-ED encompasses 124% of the National Television System Committee (NTSC) standard. These results suggest that the $CsPbX_3$@MOF-5 composites have potential benefits for WLED applications. Zhang et al. reported that the stability of $CsPbX_3$ NCs could be enhanced by incorporating them into stable Zr-based MOFs (Uio-67).[94] The $CsPbBr_3$ PNCs@Uio-67 composites showed stable PL compared to pristine $CsPbBr_3$ NCs for 30 days in air (Fig. 5c).[94] The PL emission intensity of the $CsPbBr_{1.2}/I_{1.8}$ PNCs @Uio- 67 was 67% after 30 days in air. The reduction in the PL intensity of $CsPbBr_{1.2}/I_{1.8}$ PNCs@Uio-67 might be due to structural deformation and eventual degradation under ambient atmospheric conditions.[94] The PL intensity of the $CsPbBr_3$ PNCs@Uio-67 composite displayed a thermal quenching trend with increasing temperature from 300 to 500 K. Surprisingly, the decreased PL intensity of the $CsPbBr_3$ PNCs@Uio-67 composites might have been regained, preserving 98% of the initial intensity after cooling down to room temperature. The ultimate PL intensity of $CsPbBr_3$ PNCs @Uio-67 might be able to maintain 85% of its initial value even after nine cycles.[94] The improved thermal stability might be due to the proper encapsulation of $CsPbBr_3$ PNCs in the Uio-67 porous structure.[94] WLEDs were manufactured by integrating CsPbBr3@Uio-67 composites and commercial $K_2SiF_6:Mn^{4+}$ red phosphors with a blue-emitting chip. The fabricated white LED demonstrated a CIE of (0.3690, 0.3437), CCT of 4082 K, and wide color gamut covering 138% of the NTSC standard.[94]

$CsPbBr_3$ PNCs were embedded in a small pore size LTA zeolite (0.41 nm) to impede the degradation of luminescence properties and improve their stability under various atmospheric conditions.[95] The prepared $CsPbBr_3$ PNCs@LTA zeolite exhibited a PL QY of ∼66%, which remained unchanged even after being held in air for 17 months, indicating extremely high stability (Fig. 5d).[95] The relative PL intensity of $CsPbBr_3$ PNCs@LTA was 78% of its original value after being soaked in water for 554 days (Figs. 6a and 6b), while the pristine $CsPbBr_3$ PNCs were completely decomposed in water for 72 h. It is difficult for moisture and water molecules to enter the body of the LTA zeolite because of its small pore size, which leads to the superior water stability of the $CsPbBr_3$ PNCs@LTA zeolite.[95] The PL intensity of the $CsPbBr_3$ PNCs@LTA zeolite was preserved at 100% after continuous 450 nm LED exposure for 20 days (Fig. 6c), indicating strong photostability. The decrease in the PL intensity of the $CsPbBr_3$ PNCs@LTA zeolite and $CsPbBr_3$ PNCs

Table V. Progress in $CsPbX_3$-based WLED performance.

PNCs	Encapsulation/Protection coating layer	I_F (mA)	CRI	LE (lm W^{-1})	(x, y)	Tc (K)	NTSC (%)	References.
			Metal ions doping					
$CsPbBr_3$	Zn^{2+} metal doping	N/A	N/A	36	(0.327, 0.336)	5760	137	79
$CsPbCl_3$	Sm^{3+} ion doping	N/A	93	N/A	(0.32, 0.31)	N/A	N/A	80
$CsPbBr_3$	Sn^{2+} ion doping	N/A	89	43.2	(0.41, 0.48)	3954	NA	81
$CsPbCl_3$	Mn^{2+} ion doping	N/A	67.9	2.17	(0.3930, 0.2988)	2810	NA	119
$CsPbCl_3$	Mn^{2+} ion doping	15	80	20.8	(0.334, 0.297)	5311	N/A	82
$CsPbBr_{2.2}Cl_{0.8}$	Tm^{3+}/Mn^{2+} ion doping	N/A	91	N/A	(0.33, 0.34)	N/A	N/A	83
$CsPbCl_{1.8}Br_{1.2}$	Ce^{3+}/Mn^{2+} ion co-doping/PS	N/A	89	51	(0.33, 0.29)	N/A	N/A	120
$CsPbCl_{3-x}Br_x$	Mn/ Cu co-doping	10	77	75	(0.321, 0.311)	6393	N/A	121
			Inorganic layers/SiO_2					
Mn-doped $CsPbBr_{0.5}I_{2.5}$	SiO_2	NA	60.1	19.8	(0.3327, 0.3688)	5498	N/A	58
DDAB-$CsPbBr_3$	SiO_2	30	85.3	NA	(0.35, 0.348)	5274	NA	16
$CsPbBr_3$	SiO_2	20	54.3	22.6	(0.31, 0.34)	NA	NA	14
$CsPbBr_3$	SiO2		91	32.5	(0.33, 0.38)	5218		60
$CsPbBr_3$	dual-shell SiO_2	100	82	94	(0.36, 0.35)	4448	136	62
$CsPbX_3$	SiO_2/PMMA	20	84.7	39.2	(0.349, 0.350)	4821	121.47	17
$CsPbBr_3$	$FSiO_2$/PPDMS	20	52.9	10.7	(0.33, 0.33)	5235		59
$CsPb(Br/I)_3$	SiO_2 (APTES)	20		61.2	(0.33, 0.33)		120	65
Mn-Doped $CsPbCl_3$	SiO_2 (APTES)	20	82	77.59	(0.392, 0.401)	3950		66
$CsPbX_3$	CA-SiO_2	20		26.3	(0.3225, 0.3468)			68
Mn-doped $CsPbCl_3$	SiO_2/Al_2O_3	20	83.8	80.91 1	(0.3751 0.3677)	4082		57
$CsPbBr_1I_2$	Mica		75.8	116.5	(0.6919, 0.3028)	5949	115.7	15
	Glass matrix							
$CsPbBr_3/Cs_4PbBr_6$	borosilicate glass	90	NA	78.98	(0.3195, 0.3262)	6154		85
$CsPbBr_3/Cs_4PbBr_6$	borosilicate glass	100	NA	25	(0.3328, 0.3442)	NA	130	86
$CsPbBr_3$	TeO_2-based glass		92	50−60	(0.33, 0.35)	5600		90
Rb^+-doped $CsPbBr_3$	borosilicate glass		73.4	24.60	(0.3275, 0.3303)	5732		91
Eu^{3+}-doped $CsPbBr_{1.5}I_{1.5}$	zinc borosilicate glass	20	92.4	NA	(0.3305, 0.3456)	5656		117
Mn-doped $CsPb(Cl/Br)_3$	zinc borosilicate glass	20	81.4	67	(0.3553, 0.3745)	4902		115
Zn-doped $CsPbBr_3$	borosilicate glass	NA	76.9	72.79	(0.3314, 0.3437)	NA		114
Tb^{3+} Eu^{3+} -$CsPbBr_3$	borosilicate glass	20	85.7	63.21	(0.3335, 0.3413)	4945		113
			Porous/Metal–Organic Frames (MOFs)					
$CsPbBr_3$	ZIF-8			11.5	(0.297, 0.299)	8000		92
$CsPbX_3$	MOF-5	200	83	21.6	(0.375, 0.321)	3607	124	93
$CsPbBrI_2$	zeolite/PMMA	10	94.5	77.22	(0.3359, 0.3455)	5354		96
$CsPbBr_3$	zeolite - Y	20		2 1	(0.38,0.37)	3876	114	122
$CsPbBr_3$	Uio-67				(0.3690, 0.3437)	4082	138	94
Mn^{2+} -$CsPb(Cl_{0.5}, Br_{0.5})_3$	Zeolite-Y	200	81	N/A	(0.34, 0.36)	5336	N/A	123
			Polymer Coating					
$CsPbBr_3$	POSS	20	81	14.1	(0.349, 0.383)	NA	NA	74
$CsPbBr_3$	TDPA	20	83	63	(0.31, 0.29)	7072	122	97
$CsPb(Br_xI_{1-x})_3$	PS			55.3	(0.3603, 0.2384)	2976		101
$CsPbX_3$	SBS fibers	10		9	(0.3330 0.3647)	5484	105	98
$CsPbI_3$	SEBS	NA	82.6	NA	(0.35, 0.36)	4784		102
$CsPbBr_3$	UVR	7.9	85	349	(0.33, 0.39)	5623		103
$CsPbBr_3$	PMAO	20		56.6	(0.390, 0.332)	3320		107
$CsPbBr_3$	CPB@SHFW	20		50	(0.329, 0.305)		127	108

Table V. (Continued).

PNCs	Encapsulation/Protection coating layer	I_F (mA)	CRI	LE (lm W^{-1})	(x, y)	Tc (K)	NTSC (%)	References.
$CsPbBr_3$	PMMA	20		32	(0.336, 0.342)	5318	126.55	106
$CsPbBr_3$	PMMA	10	82	35.2	(0.383, 0.323)			105
$CsPbBr_3$	CNCs-$CsPbBr_3$@PVDF				(0.0703, 0.5139)			109
$CsPbBr_3$	PDPEP-co-S	5		90	(0.31, 0.32)			110
$CsPbBr_{1.2}I_{1.8}$	SBA-15-PMMA	10			(0.722, 0.278)		135	111
$CsPbBr_{1.5}I_{1.5}$	metal stearate	30	89.9	56.54	(0.35, 0.33)	4588	N/A	112

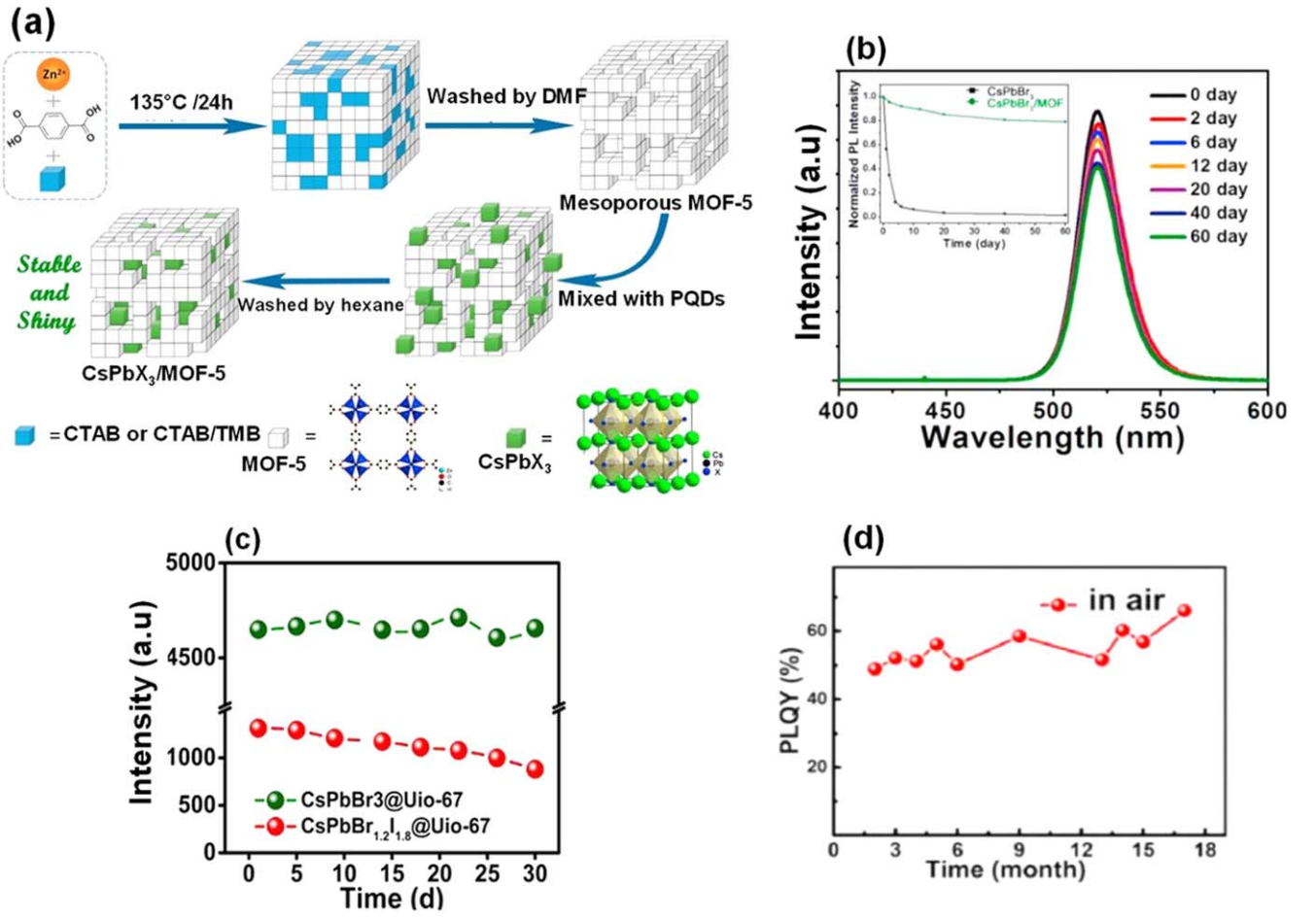

Figure 5. (a) Synthesis strategy of the mesoporous MOF-5 crystals and the $CsPbX_3$ NCs@MOF-5 composites.[93] (b) Long-term storage stability test of $CsPbBr_3$ NCs@MOF-5. Insets: normalized PL intensity as a function storage time.[93] (c) PL spectra of $CsPbBr_3$ NCs@Uio-67 and $CsPbBr_{1.2}I_{1.8}$ NCs@Uio-67 composites as a function of the storage time under atmospheric condition.[94] (d) Change in PL QY of $CsPbBr_3$ NCs@LTA in air.[95]

films increased from room temperature to 60 °C. The PL intensity remained at 57% and 35% of the starting value for $CsPbBr_3$@LTA and $CsPbBr_3$ NCs, respectively, when the temperature increased to 60 °C (Fig. 6d). This result indicates that LTA zeolite offers better encapsulation for improving the stability of $CsPbBr_3$ PNCs, which may be due to the effective suppression of thermal lattice vibration of $CsPbBr_3$ PNCs by LTA zeolite.[93]

An ion exchange study was conducted by directly mixing the $CsPbBr_3$ PNCs@LTA composite with red PNCs ($CsPbBr_{1.35}I_{1.65}$) and $CsPbBr_3$ PNCs @LTA. The peak shift does not exhibit PL characteristics, suggesting good chemical stability (Fig. 6e).[95] $CsPbX_3$ (X = Cl, Br, and I) PNCs@ZIF-8 was synthesized via a mechanical chemical synthesis process.[92] The prepared $CsPbBr_3$ PNCs@ZIF-8 composites inhibited the degradation of the luminescence properties. The PL QYs of $CsPbCl_3$ PNCs@ZIF-8, $CsPbBr_3$ PNCs@ZIF-8, and $CsPbI_3$ PNCs@ ZIF-8 composites were 51%, 72%, and 57%, respectively. The $CsPbBr_3$ PNCs@ZIF-8 composites retained 80% of the starting PL intensity under atmospheric conditions for 75 days, whereas the $CsPbBr_3$ PNCs were quenched after 15 days.[92] These results indicate that the $CsPbBr_3$ PNCs@ZIF-8 improved the stability of the PNCs. Similarly, the PL intensities of the $CsPbCl_3$ PNCs@ZIF-8 and $CsPbI_3$ PNCs@ZIF-8 composites were maintained at 48% and 71% of the starting PL intensity after 60 days of air exposure.[92] The change in the PL intensity of PNCs might be due to structural deformation and was eventually degraded under moisture conditions.[92] Compared to the initial PL intensity of the $CsPbBr_3$ PNCs @ZIF-8 and $CsPbBr_3$ PNCs, 80% and 15% were retained after continuous 365 nm UV lamp exposure for 72 h. Ion exchange was conducted by mixing $CsPbBr_3$ PNCs @ZIF-8 with $CsPbI_3$ PNCs@ZIF-8 for 30 min. The peak position and intensity of the PL peaks of the mixed samples did not change, indicating that ZIF-8 could inhibit the ion exchange process of the PNCs. Furthermore, the prepared $CsPbX_3$ PNCs@ZIF-8 composites were utilized for WLED applications.[92] The fabricated WLED displays a CCT of 8000 K, LE of 11.5 lm W^{-1}, and the CIE coordinates of the green and white LEDs were (0.130, 0.746) and (0.297, 0.299), respectively.[92] These results verified that $CsPbX_3$ PNCs/ZIF-8 composites are promising materials for WLED applications.[92] Tong et al. proposed a dual-encapsulation approach to manufacture $CsPbBrI_2$ PNCs@zeolite/PMMA composite films.[96] The dual-encapsulation approach reduced the agglomeration of PNCs and resulted in superior luminescence properties and improved environmental stability.[96] The fabricated $CsPbBrI_2$ PNCs @zeolite/PMMA composite film demonstrated a PL QY of 53.9%. The WLEDs were fabricated using a red-emitting $CsPbBrI_2$ PNCs @zeolite/PMMA composite. The fabricated WLEDs display a CRI of 94.5, LE of 77.22 lm W^{-1}, CCT of 5354 K), and tunable color coordinates of (0.3359–0.32912, 0.3455–0.3336).[96]

The stability of the luminescence properties and white PLED performance of $CsPbX_3$ NCs/NCs embedded in various MOF-porous materials are summarized in Table IV and V. MOFs have been demonstrated as efficient hosts for the encapsulation of PNCs. However, the PL QYs of the PNCs embedded into MOF hosts were lower, which could be attributed to the relatively low loading yield of PNCs in MOF hosts, and the absent or insufficient surface passivation.[93,128] Hence, developing new methods for efficiently introducing or immobilizing perovskite precursors into MOFs is necessary.[128] The detailed interaction between PNCs and MOFs

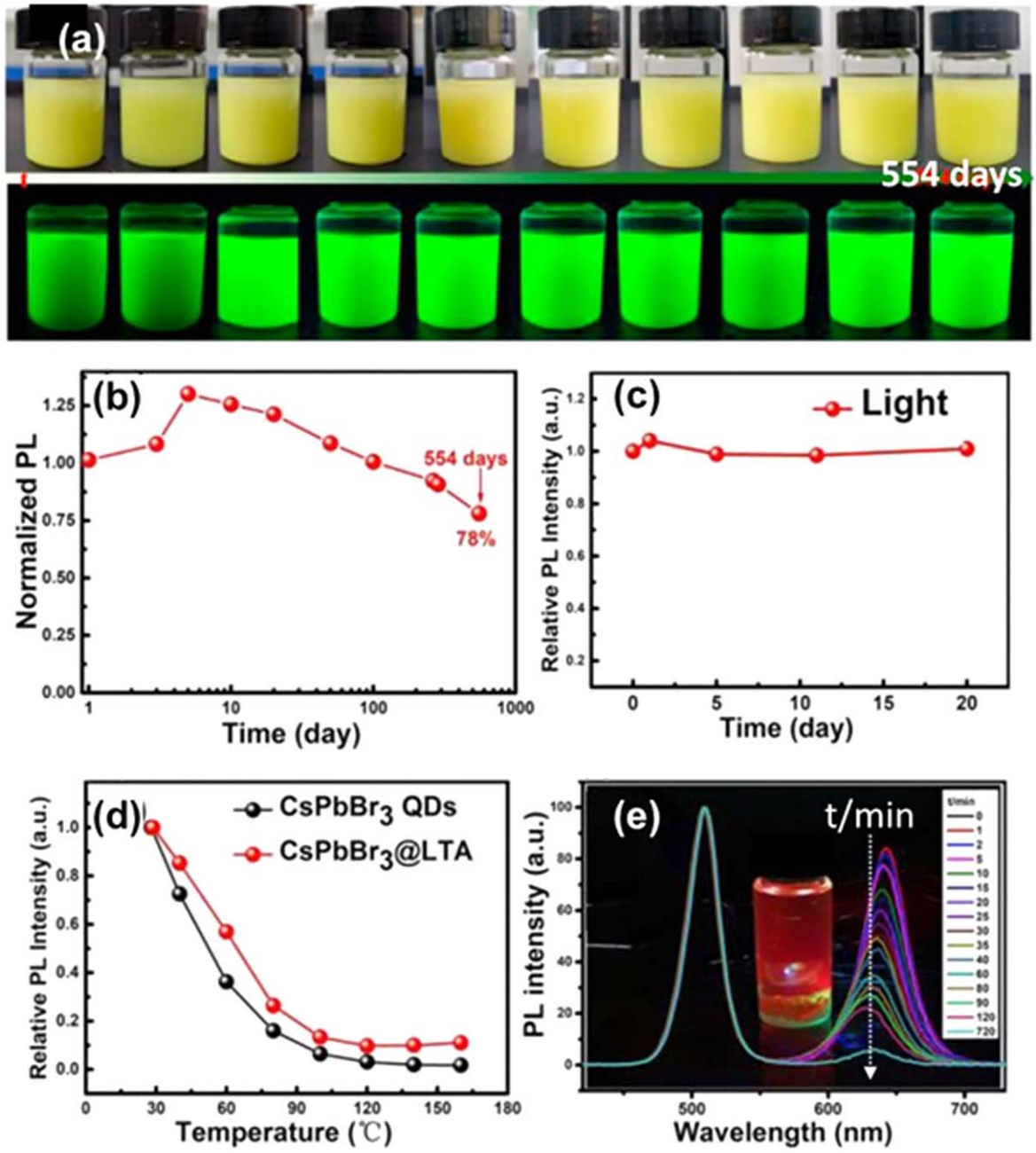

Figure 6. (a) Water stability of $CsPbBr_3$ NCs@LTA (upper images are daylight photographs, lower images are fluorescent lamp photographs).[95] (b) Normalized PL intensity of $CsPbBr_3$ NCs@LTA immersed in water for various times.[95] (c) Change in $CsPbBr_3$ NCs@LTA PL with light time.[95] (d) Change in $CsPbBr_3$ NCs@LTA PL with temperature (thermal stability).[95] (e) Chemical stability of $CsPbBr_3$ NCs@LTA (20 mg) stored in 4 ml toluene with 30 ml $CsPbBr_{1.35}I_{1.65}$ NCs.[95]

should be further studied to better design highly luminescent PNCs@MOF composites.[93] Using additional surface ligands into the PNCs@MOF composite or promoting the surface passivation effect of metal nodes or organic linkers of MOFs on the PNC surface might result in higher PL QYs.[128] Owing to the porous nature of MOFs, PNCs@MOF composites cannot survive in acidic environments with low pH, long-term exposure to high moisture, or high-energy light illumination.[128] The dual encapsulation of PNCs/QDs/MOFs/PMMA or oxide layers could be an efficient method to improve their stability.[96,128]

Polymer coating.—Polymers have many advantages, including simple processability, low density, and high flexibility, for encapsulating or passivating $CsPbX_3$ NCs.[14,130–132] Dense polymer chains can passivate the surface of perovskite and avoid direct contact with the environment.[14,130–132] Several polymers including, PMMA,[105,106,130,132,133] poly butyl methacrylate (PBMA),[130] polystyrene (PS),[100,101,130,132] poly(maleic anhydride-alt-1-octadecene) (PMA),[134] poly(maleic anhydride-alt-1-octadecene) (PMAO),[107,135] poly(vinylidene difluoride) (PVDF),[104] poly-diphenyl vinylphosphine-styrene copolymer (PDPEP-co-S),[110] epoxy resin (ER),[118] UV resin,[103] poly(styrene-butadiene-styrene) (SBS),[132] poly(L-lactic acid) (PLLA),[136] polyethylene oxide (PEO), superhydrophobic porous organic polymer frameworks (SHFW),[108] thermoplastic polyurethane (TPU),[137] polyvinylpyrrolidone (PVP),[138] styrene-ethylene-butylene-styrene (SEBS), ethyl acetate (EA),[139] ethylene vinyl acetate (EVA),[131] and others have been utilized as encapsulating or passivating layers for $CsPbX_3$ NCs.[14,99] The stability of the

luminescence properties and WLED performance of polymer-passivated $CsPbX_3$ NCs are summarized in Table IV and 5.

Wu et al. reported stable $CsPbBr_3$ PNCs with a thick (~25 nm) PMAO coating via an effective postsynthetic strategy.[107] PMAO with long hydrophobic alkyl chains bound to the surface ligands of PNCs functions as a protective layer to efficiently impede perovskite degradation from the external environment. A schematic diagram of the postsynthetic strategy for the protective PMAO polymer layer for $CsPbBr_3$ PNCs is shown in Fig. 7a.[107] The PL QYs of the prepared $CsPbBr_3$/PMAO NC composites were 88.8%. A slight decrease in the PL intensity of the $CsPbBr_3$/PMAO NC composites was observed after 40 days of air exposure, whereas the PL intensity of the pristine $CsPbBr_3$ NCs was reduced by nearly half (Fig. 7b). The $CsPbBr_3$/PMAO NC composites retained more than 90% of their initial PL intensity after continuous exposure to a 365 nm UV lamp for 144 h (Fig. 7c), whereas that of the pristine $CsPbBr_3$ PNCs was reduced to ~6% of its initial intensity (Fig. 7c). Owing to the hydrophobic nature of the polymer, $CsPbBr_3$/PMAO NCs display considerably enhanced water resistance.[107] The pristine $CsPbBr_3$ PNCs were immediately quenched in water within a few minutes, whereas the PL intensity of the $CsPbBr_3$/PMAO NCs remained at ~60% even after 24 h. These results may be attributed to the fact that the thick PMAO polymer forms a steric barrier that suppresses the structural damage of inorganic PNCs.[107] The prepared $CsPbBr_3$/PMAO NCs were coupled with a commercially available red-emitting phosphor on a blue InGaN chip to construct a WLED. The fabricated WLED exhibited a maximum LE of 56.6 lm W^{-1}, CIE coordinates of (0.390, 0.332), and CCT value of 3320 K.[107] Figure 7d shows uniform white emission from the photograph of the $CsPbBr_3$/PMAO NC-based WLED output recorded at a current of 20 mA.[107] These results demonstrate that the $CsPbBr_3$/PMAO NC-based WLED also shows improved stability compared to that of the white device with the pristine $CsPbBr_3$ PNCs. Yang et al. suggested a new synthesis route for encapsulating $CsPbBr_3$ PNCs with a

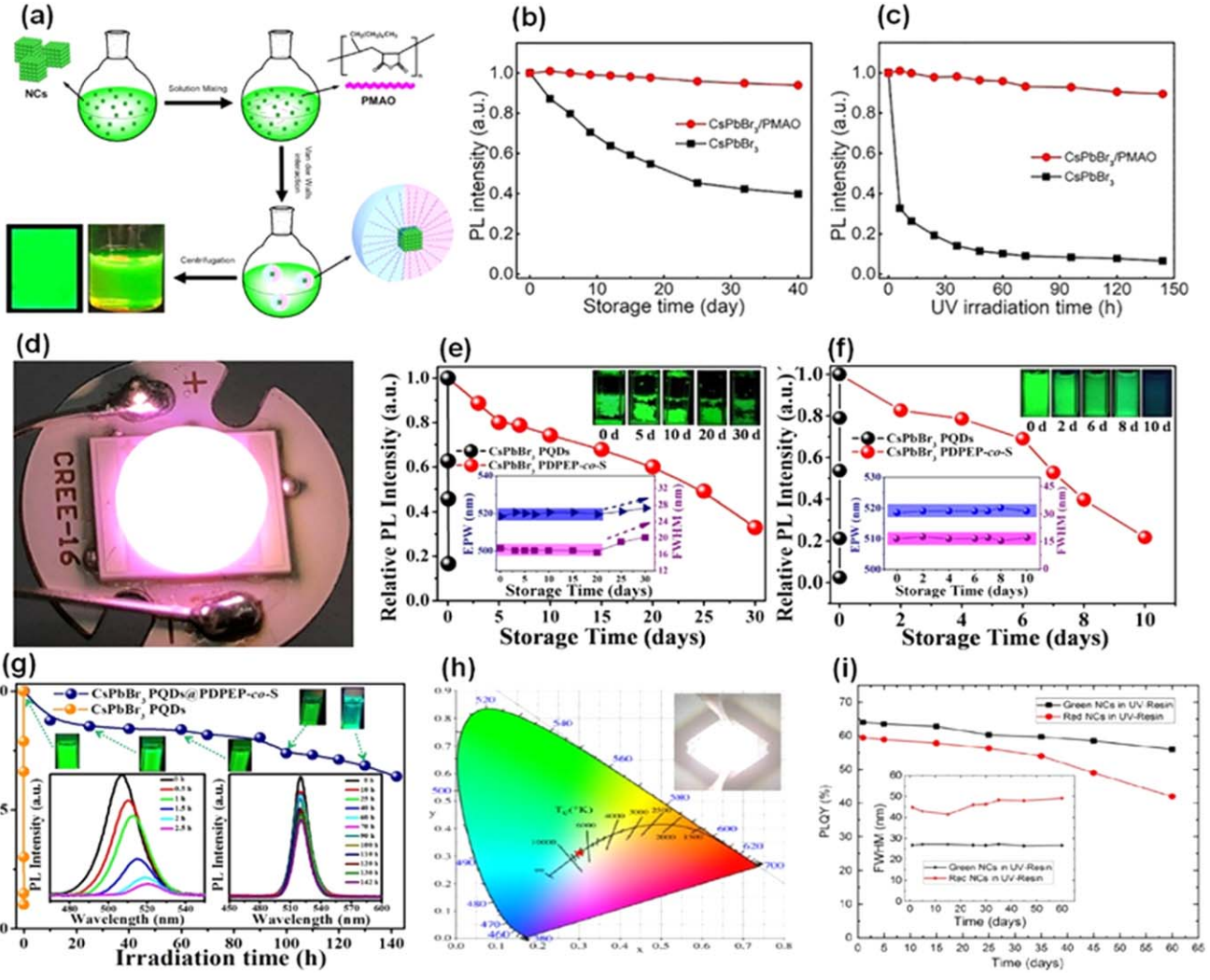

Figure 7. (a) Schematic diagram of postsynthetic treatment for obtaining PNCs with a thick PMAO polymer coating layer.[107] (b) Stability of $CsPbBr_3$ PNCs and $CsPbBr_3$ NCs @PMAO composites in the air,[107] and (c) photostability of $CsPbBr_3$ PNCs and $CsPbBr_3$ PNCs @PMAO composites,[107] (d) photograph of a working $CsPbBr_3$ PNCs @PMAO based WLED at 20 mA current.[107] (e) Relative PL intensity of pure $CsPbBr_3$ NCs and $CsPbBr_3$ NCs @PDPEP-co-S composites in deionized water monitored at different time intervals.[110] The insets are the FWHM and EPW of $CsPbBr_3$ PNCs @PDPEP-co-S composites vs the different time intervals and corresponding optical photographs.[110] (f) Relative PL intensity of pure $CsPbBr_3$ PNCs and $CsPbBr_3$@PDPEP-co-S composites in methanol monitored at different time intervals. Insets are the FWHM and EPW of $CsPbBr_3$ PNCs @PDPEP-co-S composites vs the different time intervals and corresponding optical photographs.[110] (g) Relative PL intensity of pure $CsPbBr_3$ PNCs and $CsPbBr_3$ PNCs@PDPEP-co-S composites function at different time intervals under 365-nm UV light irradiation. The insets are the original spectra with different time intervals for the pure $CsPbBr_3$ PNCs and $CsPbBr_3$ PNCs@PDPEP-co-S composites and the corresponding optical photographs.[110] (h) Color coordinates of the $CsPbBr_3$ PNCs@PDPEP-co-S composites-based WLED in the CIE 1931 diagram (Inset is the working photograph of the WLED under an injection current of 5 mA).[110] (i) Time-dependent PL QY of $CsPbBr_3$ PNCs@UVR and $CsPb(Br_{0.3}I_{0.7})_3$ PNCs@UVR composites exposed in an ambient atmosphere.[103] Inset shows the FWHM as a function of the air exposure time.[103]

PDPEP-co-S based on a one-pot hot-injection strategy.[110] The role of surface capping ligands on the PL QYs of $CsPbBr_3$ PNCs@PDPEP-co-S composites has been studied systematically.[110] A maximum PL QY of 90% was achieved for the PNCs@PDPEP-co-S - DPEP/0.6 mL composite.[110] The copolymer can efficiently prevent inner PNCs from unfavorable attacks on the surrounding environment by creating dense layers on the surface of PNCs, which avoids potential harm to the structure.[110,133] The PL intensity of pristine $CsPbBr_3$ PNCs decreased by almost 84% within 90 min in water (Fig. 7e), whereas the PL intensity of the $CsPbBr_3$ PNCs@ PDPEP-co-S composites decreased to 13% after 3 days in water (Fig. 4e). The PL emission peak wavelength (EPW) and FWHM of the $CsPbBr_3$ PNCs@PDPEP-co-S composites did not change during the first 20 days. The PL intensity of the composites was gradually reduced to 33% after 30 days in air (Fig. 7 e).[110] The hydrophobicity of PDPEP-co-S is a crucial factor in the enhancement of water stability.[110,131] When a polar solvent encounters PNCs, it may result in a huge loss of surface ligands and promote spontaneous growth of PNCs, solubility, or even optical loss.[110] However, the PDPEP-co-S framework had stronger bonding with Pb^{2+} than OA and OAm, which was also found in the multidentate binding units on the $CsPbBr_3$ PNCs.

Consequently, the PDPEP-co-S framework limited the dynamic dissolubility equilibrium and preserved the stable luminescence properties. The PL intensity of the pure $CsPbBr_3$ PNCs completely disappeared after 8 min in a strongly polar organic solvent (methanol), which showed the rapid deprivation of the $CsPbBr_3$ PNCs in methanol. The $CsPbBr_3$ PNCs@PDPEP-co-S composites preserved 82% of their original intensity after 2 days in methanol (insets in Fig. 7f) and dropped to 21% of their original intensity after 10 days (Fig. 7f). The PL intensity of the pristine PNCs has declined from 100% to 10% after UV light exposure for 2.5 h. However, the PL intensity of the $CsPbBr_3$ PNCs@PDPEP-co-S composites was decreased to 85% of the original intensity after UV exposure for 25 h (Fig. 7g).[110] Thus, the $CsPbBr_3$ PNCs were still uniformly separated from each other in PDPEP-co-S, and the photo-induced regrowth of the $CsPbBr_3$ PNCs effectively suppressed the PDPEP-co-S coating. It is worth mentioning that the phosphorus atoms in the PDPEP-co-S also acted as anchor sites for PNCs, which is crucial for restricting the regrowth of PNCs. The PL intensity of the $CsPbBr_3$ PNCs@PDPEP-co-S composites retained 64% of the original PL intensity after UV exposure for 142 h, while no substantial fluctuations in the EPW and FWHM were observed (Fig. 7g). Thus, the stability of the $CsPbBr_3$ PNC PDPEP-co-S composites was improved compared with that of the pristine $CsPbBr_3$ PNCs. Furthermore, the prepared $CsPbBr_3$ PNCs@PDPEP-co-S composite was utilized for WLED applications (Fig. 7h). The fabricated WLED shows CIE coordinates of (0.31, 0.32) and LE of 90 lm W^{-}.[110] These results demonstrate a new strategy for preparing PNC composites with long-term stability, which could pave the way for the practical implementation of halide perovskites.

Adhikari et al. demonstrated the enhanced air, moisture, and photostability of $CsPbX_3$ PNCs by encapsulation in UV resin (UVR).[103] The as-prepared $CsPbBr_3$ PNCs@UVR and $CsPb(Br_{0.3}I_{0.7})_3$ PNCs@UVR composites displayed PL QYs of 64.0% and 59.5%, respectively. The time-dependent ambient storage of the PL QY is shown in Fig. 6i.[103] The FWHM values of the PL spectra did not change significantly for more than 60 days (inset Fig. 7i). The PL QY values remained over 88% and 72% of their initial values after 60 days under ambient conditions for $CsPbBr_3$ PNCs@UVR and $CsPb(Br_{0.3}I_{0.7})_3$ PNCs@UVR composites, respectively, demonstrating that the insertion of PNCs into UVR does not degrade the luminescence properties of PNCs.[103] These results illustrate the excellent ambient stability of the $CsPbX_3$ PNCs@UVR composite, which is more stable than the PNCs-PMMA, PNCs-PBMA, and PNCs-PS composites.[65,105,130] The greatest significance of using UVR is that the curing of resin is based on free radical curing acrylic compounds (acrylates) exposed to oxygen and moisture inhibition. The prepared $CsPbBr_3$PNCs@UVR/$CsPb(Br_{0.3}I_{0.7})_3$PNCs@UVR composites were utilized to construct WLEDs stacked on top of the blue LED. The fabricated WLED showed a CCT of 5623 K, a CRI of 85, and an LER of 349 lm W^{-}.[103] The $CsPbBr_3$ PNCs @UVR composite is the most effective method for stabilizing PNCs under external environmental conditions.

Summary and Outlook

This review summarizes the major recent advances in the stability of the structural and luminescence properties of $CsPbX_3$ nanocrystals. The encapsulation strategy was found to be efficient in enhancing the stability of PNCs/PNCs, with additional benefits such as a high degree of precision, good reproducibility, and low cost. The encapsulation of PNCs with protection materials, including metal ion doping, oxides, glass, polymers, and MOFs, could enhance the stability against environmental factors and simultaneously maintain their luminescence properties. Despite their remarkable stability, all these techniques require further optimization to improve the PL QYs of these composites. Glass encapsulation showed superior water stability and UV resistance. PNCs/polymer composites present an ecofriendly way to achieve higher luminescence properties and superior water resistance. However, the thermal stability of polymers is still limited. Inorganic protecting layers, such as SiO_2, Al_2O_3, and TiO_2, demonstrate better stability against light and moisture owing to their rigid and airtight molecular structures. However, these polymers and inorganic encapsulated PNCs inevitably suffer under high-temperature conditions, because heat can transfer via the solid inorganic layer toward the PNCs. MOFs have been utilized to encapsulate PNCs, but limited stability improvement was achieved, as the open pores of the MOFs leave the PNCs exposed to external environmental condition. Inorganic shield layers are dense and airtight, but heat-conductive, whereas MOFs/porous materials are thermally insulated but not airtight. Since the operation of WLEDs involves rise in temperature of the device, materials with a higher thermal stability are desired. Therefore, PNCs encapsulated within MOFs/porous materials are probably suitable passivation materials for practical white LED devices. Nevertheless, the resistance towards moisture/polar solvents needs to be realized as well for the practical applications. It is a huge challenge to overcome this contradiction to enhance the stability of PNCs under external environmental conditions. To resolve these issues, dual-encapsulation strategies such as PPDMS-protected $CsPbBr_3$PNCs/$FSiO_2$,[59] $CsPbX_3$ (X = Cl/Br, Br, and Br/I) @SiO_2/PMMA,[71] DDAB-$CsPbX_3$@SiO_2,[69,70] $CsPbBrI_2$@zeoite/PMMA,[96] $CsPbBr_3$PNCs@PDPEP-co-S,[110] passivation of $CsPbX_3$ PNCs with dual-shell hollow SiO_2,[62] compositional engineering, and inorganic protection provide double assurance, and the enhancement of the interior structure and coating of the surface have been proposed in the literature.[14,140] The double encapsulation of $CsPbX_3$ NCs with glass matrix not only further improve the stability of PNCs but also tune their emission properties.[141]

In addition, these encapsulation techniques have certain limitations. For example, the formation of passivation layers is always accompanied by byproducts such as water or alcohols, which affect the surface of PNCs and produce surface defects, thus leading to a decrease in the PLQY. Further improvement in the luminescence properties of encapsulated PNCs is possible by optimizing the encapsulation conditions. The development of encapsulation approaches and new materials is essential to precisely encapsulate PNCs at the single-particle level, enabling micro-WLED devices.

Acknowledgments

This research was supported by the Basic Science Research Program through the National Research Foundation of Korea (NRF) funded by the Ministry of Science, ICT, and Future Planning (NRF-2017R1A2B3011967, NRF-2018R1A5A1025224, 2020M3H4A3081792, 2020M3H4A3081792,

2021M3H4A1A02049634). This work was supported by the Technology Innovation Program (KEIT-20002947, 20010737) funded By the Ministry of Trade, Industry & Energy (MOTIE, Korea). This research was supported by Korea Institute for Advancement of Technology (KIAT) grant funded by Korea Government (MOTIE). (P0017012, Human Resource Development Program for Industrial Innovation).

ORCID

Won Bin Im https://orcid.org/0000-0003-2473-4714

References

1. J. Shamsi, A. S. Urban, M. Imran, L. De Trizio, and L. Manna, *Chem. Rev.*, **119**, 3296 (2019).
2. L. Protesescu, S. Yakunin, M. I. Bodnarchuk, F. Krieg, R. Caputo, C. H. Hendon, R. X. Yang, A. Walsh, and M. V. Kovalenko, *Nano Lett.*, **15**, 3692 (2015).
3. X. Ling et al., *Adv. Energy Mater.*, **9**, 1 (2019).
4. Y.-J. Lu, T. L. Shen, K.-N. Peng, P.-J. Cheng, S.-W. Chang, M.-Y. Lu, C. W. Chu, T.-F. Guo, H. A. Atwater, and A. C. S. Photonics, *ACS Photonics*, **8**, 335 (2020).
5. D. Liu, Y. Guo, M. Que, X. Yin, J. Liu, H. Xie, C. Zhang, and W. Que, *Mater. Adv.*, **2**, 856 (2021).
6. C. Pareja-Rivera, D. E. M. Aguilar, D. Barreiro-Argüelles, P. Olalde-Velasco, D. Solis-Ibarra, and J. Phys, *Energy*, **3**, 032014 (2021).
7. R. E. Brandt, J. R. Poindexter, P. Gorai, R. C. Kurchin, R. L. Z. Hoye, L. Nienhaus, M. W. B. Wilson, J. A. Polizzotti, R. Sereika, and R. Zaltauskas, *Chem. Mater.*, **29**, 4667 (2017).
8. M. A. Becker, R. Vaxenburg, G. Nedelcu, P. C. Sercel, A. Shabaev, M. J. Mehl, J. G. Michopoulos, S. G. Lambrakos, N. Bernstein, and J. L. Lyons, *Nature*, **553**, 189 (2018).
9. A. Dutta, R. K. Behera, P. Pal, S. Baitalik, and N. Pradhan, *Angew. Chemie Int. Ed.*, **58**, 5552 (2019).
10. C. C. Stoumpos, C. D. Malliakas, and M. G. Kanatzidis, *Inorg. Chem.*, **52**, 9019 (2013).
11. Y. Dong et al., *Nat. Nanotechnol.* , **15**, 668 (2020).
12. Z. Zhu, Q. Sun, Z. Zhang, J. Dai, G. Xing, S. Li, X. Huang, and W. Huang, *J. Mater. Chem. C*, **6**, 10121 (2018).
13. M. Xia, J. Luo, C. Chen, H. Liu, and J. Tang, *Adv. Opt. Mater.*, **7**, 1 (2019).
14. W. Lv, L. Li, M. Xu, J. Hong, X. Tang, L. Xu, Y. Wu, R. Zhu, R. Chen, and W. Huang, *Adv. Mater.*, **31**, 1 (2019).
15. Q. Dong, L. Lei, J. Mendes, and F. So, *J. Phys. Mater.*, **3**, 012002 (2020).
16. F. Zhang, Z.-F. Shi, Z.-Z. Ma, Y. Li, S. Li, D. Wu, T.-T. Xu, X.-J. Li, C.-X. Shan, and G.-T. Du, *Nanoscale*, **10**, 20131 (2018).
17. H. Hu, L. Wu, Y. Tan, Q. Zhong, M. Chen, Y. Qiu, D. Yang, B. Sun, Q. Zhang, and Y. Yin, *J. Am. Chem. Soc.*, **140**, 406 (2018).
18. V. M. Goldschmidt, *Naturwissenschaften*, **14**, 477 (1926).
19. O. Nazarenko, M. R. Kotyrba, S. Yakunin, M. Aebli, G. Rainò, B. M. Benin, M. Wörle, and M. V. Kovalenko, *J. Am. Chem. Soc.*, **140**, 3850 (2018), .
20. J. P. Correa-Baena, M. Saliba, T. Buonassisi, M. Grätzel, A. Abate, W. Tress, and A. Hagfeldt, *Science*, **358**, 739 (2017).
21. Q. Sun and W.-J. Yin, *J. Am. Chem. Soc.*, **139**, 14905 (2017).
22. T. C. Jellicoe et al., *J. Am. Chem. Soc.*, **138**, 2941 (2016).
23. J.-P. Ma, J. Yin, Y.-M. Chen, Q. Zhao, Y. Zhou, H. Li, Y. Kuroiwa, C. Moriyoshi, Z.-Y. Li, and O. M. Bakr, *ACS Mater. Lett.*, **1**, 185 (2019).
24. J.-P. Ma, J.-K. Chen, J. Yin, B.-B. Zhang, Q. Zhao, Y. Kuroiwa, C. Moriyoshi, L. Hu, O. M. Bakr, and O. F. Mohammed, *ACS Mater. Lett.*, **2**, 367 (2020).
25. Q. Zhao, A. Hazarika, L. T. Schelhas, J. Liu, E. A. Gaulding, G. Li, M. Zhang, M. F. Toney, P. C. Sercel, and J. M. Luther, *ACS Energy Lett.*, **5**, 238 (2020).
26. A. Marronnier, G. Roma, S. Boyer-Richard, L. Pedesseau, J.-M. Jancu, Y. Bonnassieux, C. Katan, C. C. Stoumpos, M. G. Kanatzidis, and J. Even, *ACS Nano*, **12**, 3477 (2018).
27. A. Swarnkar, W. J. Mir, and A. Nag, *ACS Energy Lett.*, **3**, 286 (2018).
28. P. Pal, S. Saha, A. Banik, A. Sarkar, and K. Biswas, *Chem.-Eur. J*, **24**, 1811 (2018).
29. G. K. Grandhi, N. S. M. Viswanath, H. Bin Cho, J. H. Han, S. M. Kim, S. Choi, and W. Bin Im, *J. Phys. Chem. Lett.*, **11**, 7723 (2020).
30. A. Swarnkar, R. Chulliyil, V. K. Ravi, M. Irfanullah, A. Chowdhury, and A. Nag, *Angew. Chemie*, **127**, 15644 (2015).
31. R. J. Sutton, M. R. Filip, A. A. Haghighirad, N. Sakai, B. Wenger, F. Giustino, and H. J. Snaith, *ACS Energy Lett.*, **3**, 1787 (2018).
32. G. K. Grandhi, N. S. M. Viswanath, J. H. In, H. B. Cho, and W. B. Im, *J. Phys. Chem. Lett.*, **11** , 11 (2020), .
33. F. Bertolotti, L. Protesescu, M. V. Kovalenko, S. Yakunin, A. Cervellino, S. J. L. Billinge, M. W. Terban, J. S. Pedersen, N. Masciocchi, and A. Guagliardi, *ACS Nano*, **11**, 3819 (2017).
34. M. C. Brennan, M. Kuno, and S. Rouvimov, *Inorg. Chem.*, **58**, 1555 (2018).
35. D. B. Straus, S. Guo, and R. J. Cava, *J. Am. Chem. Soc.*, **141**, 11435 (2019).
36. J. Lin, M. Lai, L. Dou, C. S. Kley, H. Chen, F. Peng, J. Sun, D. Lu, S. A. Hawks, and C. Xie, *Nat. Mater.*, **17**, 261 (2018).
37. Y. Cao, G. Qi, C. Liu, L. Wang, Z. Ma, K. Wang, F. Du, G. Xiao, and B. Zou, *J. Phys. Chem. C*, **122**, 9332 (2018).
38. G. Xiao, Y. Cao, G. Qi, L. Wang, C. Liu, Z. Ma, X. Yang, Y. Sui, W. Zheng, and B. Zou, *J. Am. Chem. Soc.*, **139**, 10087 (2017).
39. J.-K. Sun, S. Huang, X.-Z. Liu, Q. Xu, Q.-H. Zhang, W.-J. Jiang, D.-J. Xue, J.-C. Xu, J.-Y. Ma, and J. Ding, *J. Am. Chem. Soc.*, **140**, 11705 (2018).
40. O. M. B. Jun Pan et al., *J. Am. Chem. Soc.*, **140** , 562 (2018), .
41. L. Protesescu et al., *ACS Nano*, **11**, 3119 (2017).
42. Q. A. Akkerman, D. Meggiolaro, Z. Dang, F. De Angelis, and L. Manna, *ACS Energy Lett.*, **2**, 2183 (2017).
43. J. A. Steele, V. Prakasam, H. Huang, E. Solano, D. Chernyshov, J. Hofkens, and M. B. J. Roeffaers, *J. Am. Chem. Soc.*, **143** , 10500 (2021), .
44. S. Kajal, G.-H. Kim, C. W. Myung, Y. S. Shin, J. Kim, J. Jeong, A. Jana, J. Y. Kim, and K. S. Kim, *J. Mater. Chem. A*, **7**, 21740 (2019).
45. S. ten Brinck and I. Infante, *ACS Energy Lett.*, **1**, 1266 (2016).
46. V. K. Ravi, P. K. Santra, N. Joshi, J. Chugh, S. K. Singh, H. Rensmo, P. Ghosh, and A. Nag, *J. Phys. Chem. Lett.*, **8**, 4988 (2017).
47. Y. Chen, S. R. Smock, A. H. Flintgruber, F. A. Perras, R. L. Brutchey, and A. J. Rossini, *J. Am. Chem. Soc.*, **142**, 6117 (2020).
48. Y. Tong, E. Bladt, M. F. Aygüler, A. Manzi, K. Z. Milowska, V. A. Hintermayr, P. Docampo, S. Bals, A. S. Urban, and L. Polavarapu, *Angew. Chemie Int. Ed.*, **55**, 13887 (2016).
49. M. I. Bodnarchuk, S. C. Boehme, S. Ten Brinck, C. Bernasconi, Y. Shynkarenko, F. Krieg, R. Widmer, B. Aeschlimann, D. Günthe, and M. V. Kovalenko, *ACS Energy Lett.*, **4**, 63 (2018).
50. J. De Roo, M. Ibáñez, P. Geiregat, G. Nedelcu, W. Walravens, J. Maes, J. C. Martins, I. Van Driessche, M. V. Kovalenko, and Z. Hens, *ACS Nano*, **10**, 2071 (2016).
51. F. Krieg et al., *ACS Energy Lett.*, **3**, 641 (2018).
52. S. R. Smock, T. J. Williams, and R. L. Brutchey, *Angew. Chemie Int. Ed.*, **57**, 11711 (2018).
53. D. Yang, X. Li, W. Zhou, S. Zhang, C. Meng, Y. Wu, Y. Wang, and H. Zeng, *Adv. Mater.*, **31**, 1900767 (2019).
54. A. Dutta, S. K. Dutta, S. Das Adhikari, and N. Pradhan, *Angew. Chemie - Int. Ed.*, **57**, 9083 (2018).
55. R. Bose et al., *ACS Appl. Mater. Interfaces*, **12**, 35598 (2020).
56. Z. Li, L. Kong, S. Huang, and L. Li, *Angew. Chemie - Int. Ed.*, **56**, 8134 (2017).
57. M. He, Y. Cheng, L. Shen, C. Shen, H. Zhang, W. Xiang, and X. Liang, *Appl. Surf. Sci.*, **448**, 400 (2018).
58. M. He, S. Liu, L. Ding, Z. Zhang, J. Liu, W. Xiang, and X. Liang, *J. Am. Ceram. Soc.*, **102**, 930 (2019).
59. S. Tu, M. Chen, and L. Wu, *Chem. Eng. J.*, **412**, 128688 (2021).
60. N. Ding, D. Zhou, X. Sun, W. Xu, H. Xu, G. Pan, D. Li, S. Zhang, B. Dong, and H. Song, *Nanotechnology*, **60**, 345703 (2018).
61. A. Pan, M. J. Jurow, Y. Wu, M. Jia, F. Zheng, Y. Zhang, L. He, and Y. Liu, *ACS Appl. Nano Mater.*, **2**, 258 (2019).
62. L. Qiu, H. Yang, Z. Dai, F. Sun, J. Hao, M. Guan, P. Dang, C. Yan, J. Lin, and G. Li, *Inorg. Chem. Front.*, **7**, 2060 (2020).
63. X. Liang, M. Chen, Q. Wang, S. Guo, and H. Yang, *Angew. Chemie*, **131**, 2825 (2019).
64. Z. Liu et al., *ACS Appl. Mater. Interfaces*, **10**, 13053 (2018).
65. C. Sun, Y. Zhang, C. Ruan, C. Yin, X. Wang, Y. Wang, and W. W. Yu, *Adv. Mater.*, **28**, 10088 (2016).
66. W. Chen, T. Shi, J. Du, Z. Zang, Z. Yao, M. Li, K. Sun, W. Hu, Y. Leng, and X. Tang, *ACS Appl. Mater. Interfaces*, **10**, 43978 (2018).
67. S. C. Hsu et al., *ACS Omega*, **6**, 2836 (2021).
68. A. Pan, Y. Li, Y. Wu, K. Yan, M. J. Jurow, Y. Liu, and L. He, *Mater. Chem. Front.*, **3**, 414 (2019).
69. X. Li, W. Cai, H. Guan, S. Zhao, S. Cao, C. Chen, M. Liu, and Z. Zang, *Chem. Eng. J.*, **419**, 129551 (2021).
70. L. Zhu, C. Wu, S. Riaz, J. Dai, and J. Lumin, **233**, 117884 (2021).
71. V. Naresh, B. H. Kim, and N. Lee, *Nano Res.*, **14**, 1187 (2021).
72. Y. Zhou, A. Pan, C. Shi, X. Ma, M. Jia, H. Huang, D. Ren, and L. He, *Appl. Surf. Sci.*, **515**, 146004 (2020).
73. I. Torun, Y. Altintas, A. F. Yazici, E. Mutlugun, and M. S. Onses, *ACS Appl. Nano Mater.*, **2**, 1185 (2019).
74. H. Huang, B. Chen, Z. Wang, T. F. Hung, A. S. Susha, H. Zhong, and A. L. Rogach, *Chem. Sci.*, **7**, 5699 (2016).
75. Z. J. Li, E. Hofman, J. Li, A. H. Davis, C. H. Tung, L. Z. Wu, and W. Zheng, *Adv. Funct. Mater.*, **28**, 1704288 (2018), .
76. D. H. Park, J. S. Han, W. Kim, and H. S. Jang, *Dye. Pigment.*, **149**, 246 (2018).
77. Y. Zhou, C. Liu, Z. Zhao, W. Zhang, K. Li, Y. Ye, C. F. Zhu, X. G. Meng, and J. Alloys Compd, *J.Alloys Compd*, **827**, 154349 (2020).
78. A. Pan, Y. Wu, K. Yan, Y. Yu, M. J. Jurow, B. Ren, C. Zhang, S. Ding, L. He, and Y. Liu, *Inorg. Chem.*, **58** , 1 (2019), .
79. R. Chen, Y. Xu, S. Wang, C. Xia, Y. Liu, B. Yu, T. Xuan, H. Li, and J. Alloys Compd, *J.Alloys Compd.*, **866**, 158969 (2021).
80. R. Sun et al., *ACS Energy Lett.*, **5**, 2131 (2020).
81. D. Yan, Q. Mo, S. Zhao, W. Cai, and Z. Zang, *Nanoscale*, **13**, 9740 (2021).
82. H. Liu, C. Sun, Z. Gao, C. Geng, S. Shi, L. Wang, S. Su, and W. Bi, *Nanoscale Res. Lett.*, **14**, 152 (2019).
83. C. Luo, W. Li, J. Fu, and W. Yang, *Chem. Mater.*, **31**, 5616 (2019).
84. Y. Yu, Y. Zhou, Y. Zhang, Y. Zhang, X. Liu, X. Liang, J. Liu, S. Chen, and W. Xiang, *J. Lumin.*, **236**, 118129 (2021).
85. F. Zheng, B. Yang, P. Cao, X. Qian, and J. Zou, *J. Alloys Compd.*, **818**, 153307 (2020).
86. B. Yang et al., *Appl. Surf. Sci.*, **512**, 145655 (2020).
87. Q. He, Y. Zhang, Y. Yu, Y. Chen, M. Jin, E. Mei, X. Liang, L. Zhai, and W. Xiang, *Chem. Eng. J.*, **411**, 128530 (2021).

88. D. Chen, S. Yuan, X. Chen, J. Li, Q. Mao, X. Li, and J. Zhong, *J. Mater. Chem. C*, **6**, 6832 (2018).
89. J. Jiang, G. Shao, Z. Zhang, L. Ding, H. Zhang, J. Liu, Z. Chen, W. Xiang, and X. Liang, *Chem. Commun.*, **54**, 12302 (2018).
90. S. Yuan, D. Chen, X. Li, J. Zhong, and X. Xu, *ACS Appl. Mater. Interfaces*, **10**, 18918 (2018).
91. H. Zhang, R. Yuan, M. Jin, Z. Zhang, Y. Yu, W. Xiang, and X. Liang, *J. Eur. Ceram. Soc.*, **40**, 94 (2020).
92. Y. Zhao, C. Xie, X. Zhang, and P. Yang, *ACS Appl. Nano Mater.*, **4**, 5478 (2021).
93. J. Ren, T. Li, X. Zhou, X. Dong, A. V. Shorokhov, M. B. Semenov, V. D. Krevchik, and Y. Wang, *Chem. Eng. J.*, **358**, 30 (2019).
94. D. Zhang, J. Zhao, Q. Liu, and Z. Xia, *Inorg. Chem.*, **58**, 1690 (2019).
95. W. Wang, R. Guo, X. Xiong, H. Liu, W. Chen, S. Hu, E. Amador, B. Chen, X. Zhang, and L. Wang, *Mater. Today Phys.*, **18**, 100374 (2021), .
96. Y. Tong, M. Jin, Y. Chen, Y. Zhao, H. Yang, Q. Wang, L. Zhai, X. Liang, and W. Xiang, *J. Mater. Chem. C*, **9**, 2530 (2021).
97. T. Xuan, X. Yang, S. Lou, J. Huang, Y. Liu, J. Yu, H. Li, K. L. Wong, C. Wang, and J. Wang, *Nanoscale*, **9**, 15286 (2017).
98. C. C. Lin, D. H. Jiang, C. C. Kuo, C. J. Cho, Y. H. Tsai, T. Satoh, and C. Su, *ACS Appl. Mater. Interfaces*, **10**, 2210 (2018).
99. Y. C. Wong, J. De Andrew Ng, and Z. K. Tan, *Adv. Mater.*, **30**, 1 (2018).
100. Y. Wei, X. Deng, Z. Xie, X. Cai, S. Liang, P. Ma, Z. Hou, Z. Cheng, and J. Lin, *Adv. Funct. Mater.*, **27**, 1703535 (2017).
101. Y. Li, J. Qian, D. Zhao, R. Song, and R. S. C. Adv, *RSC Adv.*, **11**, 18432 (2021).
102. C. Chen, Y. Wu, Z.-G. Zhu, W. Y. Shih, and W.-H. Shih, *J. Mater. Res.*, **36** , 1 (2021), .
103. G. C. Adhikari, S. Thapa, H. Zhu, P. Zhu, and A. C. S. Appl, *ACS Appl. Electron. Mater.*, **2**, 35 (2020).
104. P. Liang, P. Zhang, A. Pan, K. Yan, Y. Zhu, M. Yang, and L. He, *ACS Appl. Mater. Interfaces*, **11**, 22786 (2019).
105. J. Zhu, Z. Xie, X. Sun, S. Zhang, G. Pan, Y. Zhu, B. Dong, X. Bai, H. Zhang, and H. Song, *ChemNanoMat*, **5**, 346 (2019).
106. Z. Wang, R. Fu, F. Li, H. Xie, P. He, Q. Sha, Z. Tang, N. Wang, and H. Zhong, *Adv. Funct. Mater.*, **31**, 2010009 (2021).
107. H. Wu, S. Wang, F. Cao, J. Zhou, Q. Wu, H. Wang, X. Li, L. Yin, and X. Yang, *Chem. Mater.*, **31**, 1936 (2019).
108. T. Xuan, J. Huang, H. Liu, S. Lou, L. Cao, W. Gan, R. S. Liu, and J. Wang, *Chem. Mater.*, **31**, 1042 (2019).
109. J. Guan, M. Song, L. Chen, Y. Shu, D. Jin, G. Fan, Q. Xu, and X. Y. Hu, *Carbon N. Y.*, **175**, 93 (2021).
110. W. Yang, L. Fei, F. Gao, W. Liu, H. Xu, L. Yang, and Y. Liu, *Chem. Eng. J.*, **387**, 124180 (2020).
111. Y. Xie, Y. Yu, J. Gong, C. Yang, P. Zeng, Y. Dong, B. Yang, R. Liang, Q. Ou, and S. Zhang, *Opt. Mater. Express*, **8**, 3494 (2018).
112. Y. Chang et al., *ACS Appl. Mater. Interfaces*, **10**, 37267 (2018).
113. Y. Cheng, C. Shen, L. Shen, W. Xiang, and X. Liang, *ACS Appl. Mater. Interfaces*, **10**, 21434 (2018).
114. L. Ding, S. Liu, Z. Zhang, G. Shao, W. Xiang, and X. Liang, *Ceram. Int.*, **45**, 22699 (2019).
115. M. He, Y. Cheng, L. Shen, H. Zhang, C. Shen, W. Xiang, and X. Liang, *J. Am. Ceram. Soc.*, **102**, 1090 (2019).
116. B. Zhang et al., *J. Alloys Compd.*, **874**, 159962 (2021).
117. R. Yuan, J. Liu, H. Zhang, Z. Zhang, G. Shao, X. Liang, and W. Xiang, *J. Am. Ceram. Soc.*, **101**, 4927 (2018).
118. S. Liu, M. He, X. Di, P. Li, W. Xiang, and X. Liang, *Chem. Eng. J.* (2017)**330**, 823.
119. M. He, Y. Cheng, R. Yuan, L. Zhou, J. Jiang, T. Xu, W. Chen, Z. Liu, W. Xiang, and X. Liang, *Dye. Pigment.*, **152**, 146 (2018).
120. G. Pan et al., *ACS Appl. Mater. Interfaces*, **10**, 39040 (2018).
121. Y. Zheng, X. Yuan, J. Yang, Q. Li, X. Yang, Y. Fan, H. Li, H. Liu, J. Zhao, and J. Lumin, *J. Lumin.*, **227**, 117586 (2020).
122. J. Y. Sun, F. T. Rabouw, X. F. Yang, X. Y. Huang, X. P. Jing, S. Ye, and Q. Y. Zhang, *Adv. Funct. Mater.*, **27** , 1704371 (2017).
123. S. Ye, J. Y. Sun, Y. H. Han, Y. Y. Zhou, and Q. Y. Zhang, *ACS Appl. Mater. Interfaces*, **10**, 24656 (2018).
124. Z. Bao, H.-D. Chiu, W. Wang, Q. Su, T. Yamada, Y.-C. Chang, S. Chen, Y. Kanemitsu, R.-J. Chung, and R.-S. Liu, *J. Phys. Chem. Lett.*, **11**, 10196 (2020).
125. B.-S. Zhu, H.-Z. Li, J. Ge, H.-D. Li, Y.-C. Yin, K.-H. Wang, C. Chen, J.-S. Yao, Q. Zhang, and H.-B. Yao, *Nanoscale*, **10**, 19262 (2018).
126. D. N. Dirin, B. M. Benin, S. Yakunin, F. Krumeich, G. Raino, R. Frison, M. V. Kovalenko, and A. C. S. Nano, *ACS Nano*, **13**, 11642 (2019).
127. S. Lou, T. Xuan, C. Yu, M. Cao, C. Xia, J. Wang, and H. Li, *J. Mater. Chem. C*, **5**, 7431 (2017).
128. C. Zhang, W. Li, and L. Li, *Angew. Chemie - Int. Ed.*, **60**, 7488 (2021).
129. B. Rungtaweevoranit, Y. Zhao, K. M. Choi, and O. M. Yaghi, *Nano Res.*, **9**, 47 (2016).
130. Y. Xin, H. Zhao, and J. Zhang, *ACS Appl. Mater. Interfaces*, **10**, 4971 (2018).
131. Y. Li, Y. Lv, Z. Guo, L. Dong, J. Zheng, C. Chai, N. Chen, Y. Lu, and C. Chen, *ACS Appl. Mater. Interfaces*, **10**, 15888 (2018).
132. D. H. Jiang, Y. H. Tsai, L. Veeramuthu, F. C. Liang, L. C. Chen, C. C. Lin, T. Satoh, S. H. Tung, and C. C. Kuo, *APL Mater.*, **7**, 111105 (2019).
133. Y. Wang, L. Varadi, A. Trinchi, J. Shen, Y. Zhu, G. Wei, and C. Li, *Small*, **14**, 1 (2018).
134. M. Meyns et al., *ACS Appl. Mater. Interfaces*, **8**, 19579 (2016).
135. J. Xu, L. Zhu, J. Chen, S. Riaz, L. Sun, Y. Wang, W. Wang, and J. Dai, *Phys. Status Solidi - Rapid Res. Lett.*, **15**, 1 (2021).
136. Y. Duan, G.-Z. Yin, D.-Y. Wang, and R. D. Costa, *ACS Appl. Mater. Interfaces*, **13**, 21800 (2021).
137. W. Ge, J. Shi, Y. Tian, M. Xu, Y. Wu, and Y. Li, *J. Alloys Compd*, **865**, 158768 (2021).
138. L. Veeramuthu, F. C. Liang, Z. X. Zhang, C. J. Cho, E. Ercan, C. C. Chueh, W. C. Chen, R. Borsali, and C. C. Kuo, *ACS Omega*, **5**, 8972 (2020).
139. M. Zhang, M. Wang, Z. Yang, J. Li, and H. Qiu, *J. Alloys Compd*, **748**, 537 (2018).
140. T. Guner and M. M. Demir, *Phys. Status Solidi Appl. Mater. Sci.*, **215**, 1 (2018).
141. Y. H. Nam, K. Han, W. J. Chung, and W. Bin Im, *ACS Appl. Nano Mater.*, **4**, 7072 (2021).